


Article

Thermal Maturity Constraint Effect and Development Model of Shale Pore Structure: A Case Study of Longmaxi Formation Shale in Southern Sichuan Basin, China

Xuewen Shi ^{1,2}, Wei Wu ^{1,2}, Liang Xu ^{1,2,*}, Yingzi Yin ^{1,2}, Yuran Yang ^{1,2}, Jia Liu ^{1,2}, Xue Yang ^{1,2}, Yanyou Li ^{1,2}, Qiuzi Wu ^{1,2}, Kesu Zhong ^{1,2} and Yonghui Wu ^{3,4,*} 

- ¹ Shale Gas Research Institute, Petrochina Southwest Oil & Gas Field Company, Chengdu 610051, China; shixuewen@petrochina.com.cn (X.S.); wuweipetrochina@163.com (W.W.); yinyingzi@petrochina.com.cn (Y.Y.); yangyuran@petrochina.com.cn (Y.Y.); liujia05@petrochina.com.cn (J.L.); yangx63@petrochina.com.cn (X.Y.); liyy_2021@petrochina.com.cn (Y.L.); 15608220826@163.com (Q.W.); zks957@petrochina.com.cn (K.Z.)
- ² Sichuan Provincial Key Laboratory of Shale Gas Evaluation and Exploitation, Chengdu 610051, China
- ³ National Key Laboratory of Petroleum Resources and Engineering, China University of Petroleum (Beijing), Beijing 102249, China
- ⁴ Unconventional Petroleum Research Institute, China University of Petroleum (Beijing), Beijing 102249, China
- * Correspondence: xul_2021@petrochina.com.cn (L.X.); yhwu1026@126.com (Y.W.)

Abstract: When the thermal maturity of the Longmaxi Formation in the southern Sichuan Basin is too high, the pore structure of shale becomes poor. Therefore, to investigate the effect of organic matter thermal maturity on shale pore structure, a study was conducted. Using the Longmaxi Formation shale in the southern Sichuan Basin as an example, the intrinsic relationship between shale porosity, pore structure parameters, organic matter laser Raman maturity, and organic matter graphitization degree was examined using X-ray photoelectron spectroscopy, particle helium porosity measurement, organic matter micro-laser Raman spectroscopy, and gas adsorption experiments. The results indicate that thermal maturity is the macroscopic manifestation of the graphitization degree of organic matter, and the correlation coefficient between the two is 0.85. A thermal maturity of 3.5% (with a corresponding organic matter graphitization degree of 17%) aligns with the highest values of shale porosity, pore volume, and pore-specific surface area across all pore size conditions. The evolution model of shale pore structure can be divided into two stages. The first stage is characterized by a thermal maturity between 2.0% and 3.5% (with a corresponding degree of graphitization of organic matter between 0% and 17%). During this stage, the number and connectivity of micro-macropores increase with increasing thermal maturity. The second stage is marked by a thermal maturity between 3.5% and 4.3% (with a corresponding degree of graphitization of organic matter between 17% and 47.32%). Basement faults are present, leading to abnormally high thermal maturity, poor preservation conditions, continuous generation of micropores, better connectivity, and a reduced number of pores. Medium macropores with good connectivity suffer from gas loss in the fracture network, leading to the collapse and disappearance of pores. The results mentioned in the statement have an important guiding role in the efficient exploration of shale gas in the Longmaxi Formation in the southern Sichuan Basin.

Keywords: southern Sichuan Basin; Longmaxi Formation; thermal maturity; pore structure; constraint effect; pattern of development



Citation: Shi, X.; Wu, W.; Xu, L.; Yin, Y.; Yang, Y.; Liu, J.; Yang, X.; Li, Y.; Wu, Q.; Zhong, K.; et al. Thermal Maturity Constraint Effect and Development Model of Shale Pore Structure: A Case Study of Longmaxi Formation Shale in Southern Sichuan Basin, China. *Minerals* **2024**, *14*, 163. <https://doi.org/10.3390/min14020163>

Academic Editors: Luca Aldega and Thomas Gentzis

Received: 20 November 2023

Revised: 25 January 2024

Accepted: 29 January 2024

Published: 2 February 2024



Copyright: © 2024 by the authors. Licensee MDPI, Basel, Switzerland. This article is an open access article distributed under the terms and conditions of the Creative Commons Attribution (CC BY) license (<https://creativecommons.org/licenses/by/4.0/>).

1. Introduction

In recent years, there have been significant breakthroughs in the exploration of shale gas in the Upper Ordovician Wufeng Formation–Lower Silurian Longmaxi Formation in the Sichuan Basin. This has led to the establishment of national shale gas exploration and development demonstration sectors in the Weiyuan area, Changning area, Zhaotong

area, and Fuling area, as well as in the surrounding areas of the Sichuan Basin [1]. As an unconventional oil and gas resource, the enrichment of shale gas is influenced by gas generation, reservoir, and preservation conditions [2,3]. Despite extensive studies on the gas generation conditions, reservoir conditions, and preservation conditions of shale reservoirs, there are still some gaps to be filled. For instance, during the evaluation of shale reservoirs, there is a noticeable issue with the pore structure of high-thermal-maturity shale reservoirs, and there is a lack of research in this particular area. Furthermore, the influence of thermal maturity on the pore structure of shale reservoirs is not well understood, which hinders the optimization and well location deployment in shale reservoir development.

The methods used to characterize shale thermal maturity primarily include the asphalt reflectance method, laser Raman spectroscopy, infrared spectroscopy, the graptolite reflectance method, X-ray photoelectron spectroscopy, and the transmission electron microscopy image method [4]. The maturity measured by the asphalt reflectance method depends on the optical properties of the organic matter surface. However, due to the limitations imposed by the incident light angle on the optical properties, the maturity data obtained through this method often exhibit significant variation, leading to reduced accuracy [5]. Compared with the asphalt reflectance method, laser Raman spectroscopy is relatively stable and is commonly used for shale thermal maturity characterization [6]. The graptolite reflectance method involves determining the thermal maturity of shale by measuring the reflectivity of graptolite within it. Like other optical methods, the measured results are influenced by optical properties, and the values obtained are generally lower compared to those from the asphalt reflectance method and laser Raman spectroscopy [7,8]. X-ray photoelectron spectroscopy is a method used to assess thermal maturity by analyzing the structure of carbon-containing functional groups within organic matter. This technique is commonly employed to investigate the microscopic mechanisms underlying thermal maturity [9]. Transmission electron microscopy is a powerful method for characterizing the microstructure of organic matter. It enables researchers to examine the number and orientation of lattice fringes in the image, which provides direct evidence of the changes occurring in the microstructure of organic matter. By analyzing these lattice fringes, the thermal maturity of organic matter can be determined [10].

The pore size of shale is complex, and it is divided into micropores (<2 nm), mesopores (2–50 nm), and macropores (>50 nm) according to the standards of the International Union of Pure and Applied Chemistry (IUPAC) [11]. The characterization methods of shale pore structure can be divided into direct observation methods and indirect measurement methods [12]. The direct observation methods encompass a range of techniques, including the field emission scanning electron microscope (FE-SEM) imaging method, the large field scanning electron microscope (SEM) image stitching method, the neutron small-angle scattering method, the nano-CT method, and the FIB-SEM three-dimensional image reconstruction method [13–16]. The field emission scanning electron microscope has a limited viewing angle, and a sparse collection of scanning electron microscope images may not fully capture the heterogeneity of shale samples [17]. The large-field scanning electron microscope image stitching method is an effective approach to seamlessly stitch numerous high-resolution scanning electron microscope images based on their spatial positions. This technique can effectively mitigate sample heterogeneity. However, it is worth noting that this method can be costly and does not provide three-dimensional information about the sample [16]. Neutron small-angle scattering is an experimental technique that employs elastic neutron scattering at low angles to study nanostructures ranging from one to hundreds of nanometers within materials. This technique effectively addresses the issue of insufficient resolution in existing experiments, yet it is faced with challenges related to high cost and limited availability of equipment [18]. The nano-CT method utilizes X-ray penetration to scan and generate images of small samples, allowing for the extraction of relevant information regarding pore structure through image segmentation technology. This technique offers the advantage of capturing the three-dimensional information of the samples. However, it is important to note that it may have drawbacks, such as unclear

identification of pore genetic types and a relatively high cost [19]. The FIB-SEM three-dimensional image reconstruction method involves the organic stacking of multiple large-view mosaic images in the vertical direction. This technique offers a higher resolution than the three-dimensional images generated by nano-CT and enables the identification of pore genetic types. However, it is worth noting that this method may still be limited by its relatively high cost [19]. Indirect measurement methods include the gas adsorption method, the high-pressure mercury intrusion method, and the nuclear magnetic resonance method [20–22]. The gas adsorption method primarily utilizes CO₂ and N₂. This method can characterize pores with a size of less than 2 nm using CO₂ adsorption, while N₂ adsorption is mostly employed for characterizing pore structures with a size range of 2 to 100 nm [23,24]. This method is commonly used to characterize the pore structure of shale. However, gas adsorption experiments are usually carried out at low temperatures, and the pore structures in some samples may exhibit different behaviors at room temperature or high temperature. These differences can lead to disparities between the measured results and the actual situation. The high-pressure mercury intrusion method is employed to obtain pore size distribution by displacing a wet phase with a non-wet phase. This technique is useful for characterizing the pore structure of macropores, which have a pore size greater than 50 nm [20,21]. However, the small pore size of shale, high displacement pressure, and the difficulty regarding non-wet-phase mercury penetrating the shale reservoir result in low accuracy when using the high-pressure mercury intrusion method to characterize the pore size of shale. An alternative approach is the nuclear magnetic resonance (NMR) method, which relies on the difference in hydrogen signals between saturated and dry samples to reflect pore information [25]. However, the NMR method expresses pore structure information based on the relationship between signal amplitude and transverse relaxation T₂, necessitating the conversion of relaxation rates to obtain pore size. Although some studies have explored the value of NMR relaxation rate using approaches such as adsorption proportional equations, mercury intrusion, or nitrogen calibration for T₂, the results vary considerably, leading to reduced accuracy of the method [26].

The controlling factors of shale pore structure include rock fabric, diagenesis, tectonic activity, and other factors [27–30]. The influence of rock fabric on shale pore structure is primarily discussed in terms of mineral composition and total organic carbon (the mass ratio of organic matter in unit mass rock is expressed by TOC) [27]. The influence of diagenesis on shale pore structure is commonly explored through various aspects, including the reduction in pores due to siliceous cementation, the increase in pores caused by feldspar dissolution, as well as the expansion of pores resulting from calcite and dolomite dissolution [28,29]. To analyze the control of tectonic activity on shale pore structure, researchers often examine the variation in pore structure among different structural features or regions. This approach allows for a comprehensive understanding of the impact of tectonic activity on shale pore development [30].

In summary, there are few studies addressing the influence of thermal maturity on shale pore structure. Taking into account the advantages, drawbacks, and cost-effectiveness of various methods for characterizing thermal maturity and pore structure, this paper employs organic matter laser Raman spectroscopy and X-ray photoelectron spectroscopy to assess the thermal maturity of shale and the degree of organic matter's tendency toward a graphite structure (i.e., the degree of graphitization). Additionally, shale porosity is measured using the particle helium porosity method, while CO₂ and N₂ adsorption are utilized to characterize the pore structure within the ranges of 0–2 nm and 2–100 nm, respectively. The paper analyzes the relationship between shale porosity, pore structure parameters, thermal maturity, and the degree of organic matter graphitization. Furthermore, it reveals the controlling impact of thermal maturity on shale pore structure and establishes an evolution model for shale pore structure constrained by thermal maturity.

2. Geology Settings

The study area is situated in the southern region of the Sichuan Basin and is bounded by the Emeishan–Liangshan thrust belt and the Hunan–Guizhou–Hubei thrust belt in the east–west direction. In the southwest, it is adjacent to the Kangdian ancient land, while the Qianzhong uplift lies to the south of the area [31]. During the Permian period, extensive basaltic eruptions occurred in southwestern China and northern Vietnam as a result of Emei rifting, leading to a rise in terrestrial heat flow values. This event, known as the Emeishan large igneous province, caused the premature maturation of organic matter in the shale of the Upper Ordovician Wufeng Formation and Lower Silurian Longmaxi Formation [32]. During the early and middle Cretaceous periods, the Sichuan Basin experienced its maximum ancient burial depth, leading to the highest level of thermal maturity for organic matter [33]. Near the Emeishan basalt eruption zone or the basement fault, the organic matter maturity of the Wufeng–Longmaxi shale is exceptionally high, and the shale contains an abundant presence of graphite crystal structure in its organic matter composition [34]. During the early and middle stages of the Yanshan movement, the Xuefeng uplift in the southeast margin of the Sichuan Basin experienced compression towards the northwest, resulting in the formation of numerous NE-trending ejective folds in the Luzhou area [35]. During the late Yanshan period, the study area underwent compression from north–south stress, leading to the formation of an east–west fault in Changning and its surrounding regions. This geological event also resulted in a modification in the strike of the NE-trending fault at the end in the Luzhou area [35]. During the Himalayan period, as a result of the northwestward extrusion of the Qinghai–Tibet Plateau, the Sichuan Basin experienced dextral strike-slip stress. This stress reactivated and re-affected the previously formed faults, leading to their further deformation and destruction [34,36]. The intense tectonic activities during the Yanshan and Himalayan periods significantly influenced the preservation conditions of shale gas and the distribution of favorable exploration areas for this resource (Figure 1).

During the sedimentary period of the Wufeng Formation–Longmaxi Formation shale, the study area was situated in an epicontinental sea environment, characterized by a weak source supply. This led to the deposition of organic-rich shale primarily composed of suspended sediments [37]. The Wufeng Formation–Longmaxi Formation can be split into the Wufeng Group, the Long 1 Section, and the Long 2 Section from bottom to top. The Long 1 Section can further be divided into the Long 1 subsection and the Long 2 subsection [38]. The experimental samples used in this work were taken from the Long 1 subsection, which is the principal shale gas generating stratum according to the production results [38].

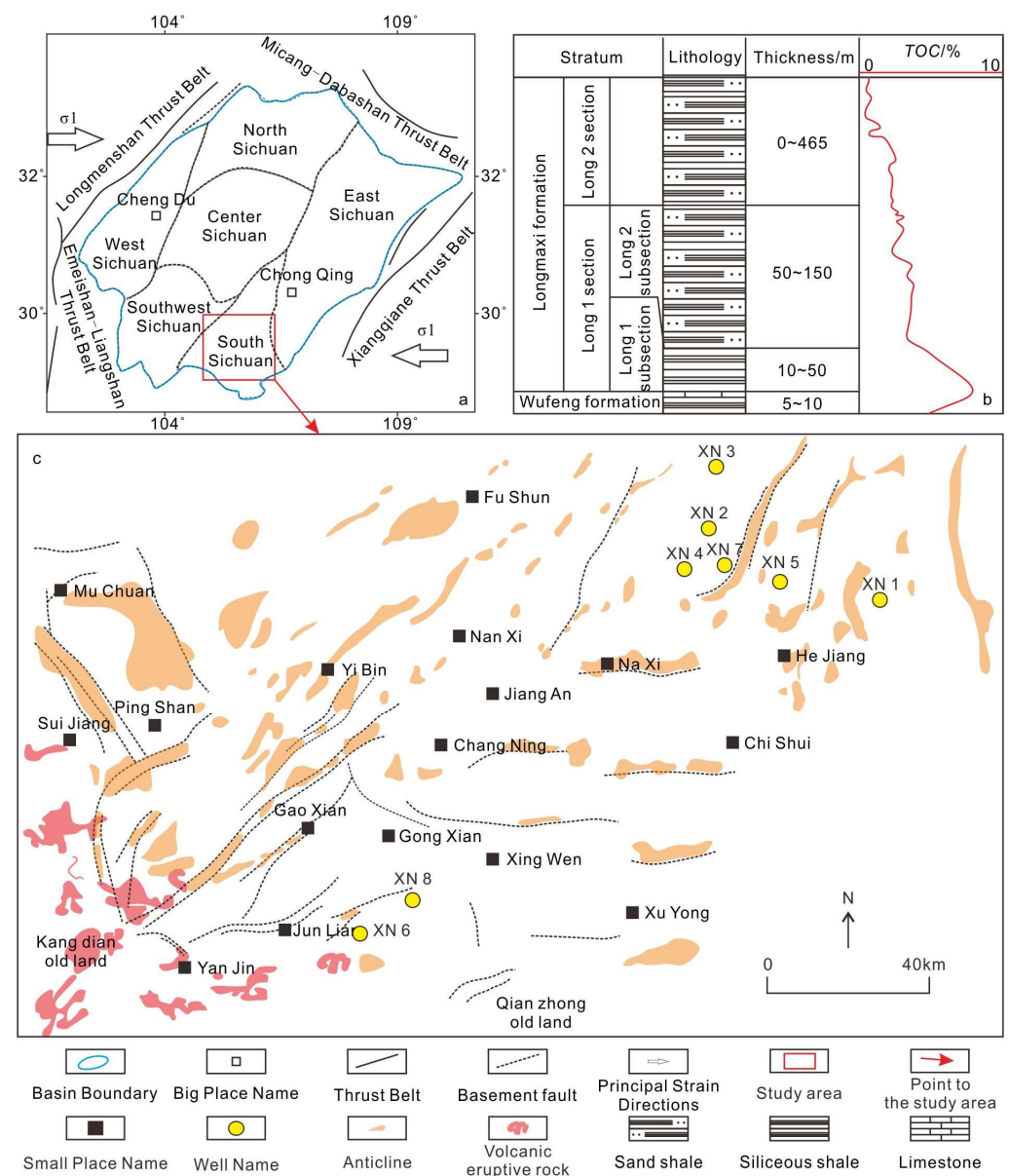


Figure 1. Geographical location and structural characteristics of the research area.

3. Samples, Data, and Methods

3.1. Samples and Data

To investigate the influence of organic matter thermal maturity on shale pore structure, two shale samples (sample Nos. XN6 and XN8) from near the Emeishan basalt eruption zone and the basement fault, and one shale sample (sample No. XN7) from the basement fault syncline, were selected based on regional geological background studies. Additionally, five shale samples (sample Nos. XN1, XN2, XN3, XN4, and XN5) from other structural locations were also included. Table 1 presents detailed information for each sample.

According to the shale lithofacies classification scheme of ‘TOC + mineral composition’ [39], it is evident that the TOC content of these 8 samples exceeds 2%, and the felsic mineral content is predominantly above 50%. Therefore, all these samples can be classified as organic-rich siliceous shale (Figure 2). Under consistent lithofacies conditions, the pore structure of shale can be considered to be influenced by tectonic activity and the thermal maturity of organic matter. Based on the regional geological background, it is observed that the thermal maturity of the syncline near the basement fault or the shale near the Emeishan basalt eruption zone exhibits abnormally high levels, suggesting a corresponding

relationship between high thermal maturity and the activity of the basement fault [34]. Based on this, under the same lithofacies conditions, the controlling factor of shale pore structure can be directly attributed to the thermal maturity of organic matter.

Table 1. Sample information form.

Sample Number	Stratum	Depth/m	TOC/%	Quartz and Feldspar/%	Carbonate/%	Clay/%	Pyrite/%
XN1	Long 1 subsection	4315.00	4.17	77.30	15.70	7.00	0.00
XN2	Long 1 subsection	4252.00	4.54	73.00	6.00	16.00	5.00
XN3	Long 1 subsection	3611.00	5.30	49.00	37.00	10.00	4.00
XN4	Long 1 subsection	4314.00	4.27	50.50	12.15	33.52	3.84
XN5	Long 1 subsection	4125.00	5.50	63.10	16.40	18.00	2.50
XN6	Long 1 subsection	2256.00	3.10	50.00	23.00	23.00	4.00
XN7	Long 1 subsection	4360.00	4.25	56.00	10.00	27.00	7.00
XN8	Long 1 subsection	2285.50	3.74	52.00	24.00	21.00	3.00

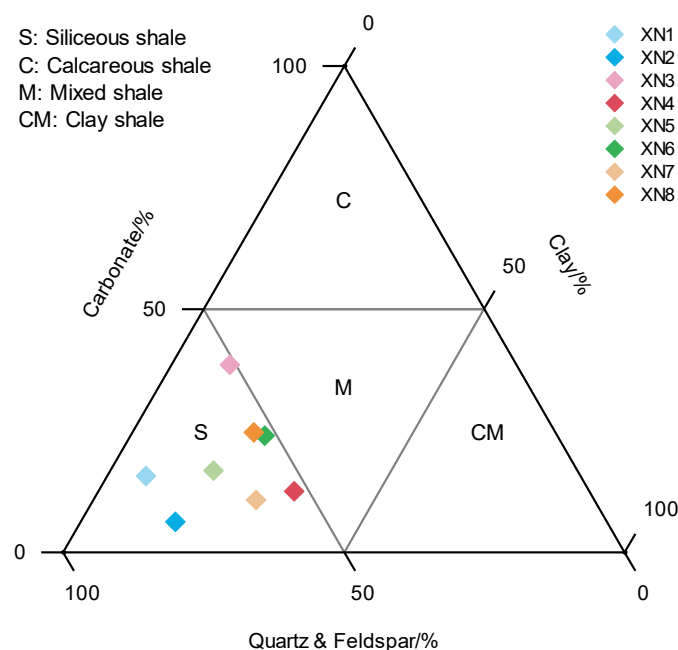


Figure 2. Shale petrographic classification diagram.

3.2. Methods

3.2.1. Laser Raman

The shale core was processed into thin slices and mechanically polished to obtain experimental samples with a flat surface. The automatic microscopic laser Raman spectrometer was (China University of Petroleum, Beijing, China) then used to test the laser Raman spectrum of the point rich in organic matter on the sample surface, thus obtaining the laser Raman spectrum of the organic matter at that specific point. Among them, the experimental test conditions include a solid-state laser operating at 532 nm with an energy output ranging from 30 to 50 mW. The laser energy is attenuated using D1–D2 method, and a grating with 1800 lines is used. The confocal pinhole size ranges from 100 to 300 μm , while the grating slit is set at 100 μm . The observation objective is set between $\times 50$ and $\times 100$ magnification, with an exposure time of 10 to 40 s. The scanning wave number range is set between 100 and 4000 cm^{-1} , and a silicon wafer is used for wave number calibration of the Raman instrument.

In the study of laser Raman spectroscopy, the maturity of organic matter can be characterized by the geometric parameters of the D peak and G peak. The Raman shift

range of the D peak is typically observed between 1250 and 1450 cm^{-1} , which provides information about the lattice structure defects and vacancies within the aromatic ring sheet. On the other hand, the Raman shift range of the G peak is commonly found between 1500 and 1605 cm^{-1} , indicating the stretching vibration of the C=C bond. For over-mature shale, the laser Raman maturity of organic matter can be quantified using the ratio of the Raman intensity of the D peak to the G peak [6]. The calculation formula is as follows:

$$R_{\text{Rmc,o}} = 1.1659 \times \frac{D_h}{G_h} + 2.7588 \quad (1)$$

In the formula, $R_{\text{Rmc,o}}$ represents the maturity of organic matter laser Raman, where D_h is the Raman intensity of the D peak, and G_h is the Raman intensity of the G peak.

Due to instrumental or environmental factors, the laser Raman spectrum's baseline may not be straight, requiring correction. In this paper, the Raman spectral curve's baseline is corrected to obtain the peak height ratio of the D peak and G peak using Origin 2018. This ratio is then utilized for the calculation of Formula (1).

3.2.2. X-ray Photoelectron Spectroscopy

X-ray photoelectron spectroscopy (XPS) can be utilized to measure the information of C, N, O, and S elements in the sample. In shale, the organic matter contains carbon, but carbonate minerals also contain carbon. To investigate the characteristics of carbon-containing functional groups in organic matter under various thermal maturity conditions, it is essential to extract the organic matter from shale samples for further analysis [23].

Before the experiment, the extracted organic matter powder was compressed into flakes. These flake samples were then analyzed using X-ray photoelectron spectroscopy (ESCALab 250 Xi) at China University of Petroleum (Beijing, China). To ensure accurate photoelectron spectroscopy of the C element, the experimental test scheme is as follows. The first step involves obtaining the comprehensive photoelectron spectroscopy of C, N, O, and S elements. The second step is to adjust the experimental parameters to specifically capture the photoelectron spectroscopy of the C element. The experimental acquisition parameters for the first step are as follows: Number of Scans: 1, Source Gun Type: A1 K Alpha, Spot Size: 300 Ω , Analyzer Mode: CAE with Pass Energy of 200.0 eV, Energy Step Size: 1.0 eV, and Number of Energy Steps: 1261. In the second step, the acquisition parameters are as follows: Number of Scans: 5, Source Gun Type: A1 K Alpha, Spot Size: 300 Ω , Analyzer Mode: CAE with Pass Energy of 50.0 eV, Energy Step Size: 0.1 eV, and Number of Energy Steps: 191.

In the over-mature stage, the carbon-containing functional groups in organic matter primarily consist of C=C, C-C, C-O, and C=O. As the degree of thermal evolution increases, organic matter tends to transform into graphite, leading to an increased proportion of C=C. Therefore, based on the C element photoelectron spectroscopy, the XPS PEAKS software (ver. 4.1) is used to fit the peaks, allowing for the identification and characterization of the photoelectron spectroscopy of each carbon-containing functional group. The position of the peak is determined by the binding energy of the functional group. Specifically, the peak position of C=C is at 284.3 eV, the peak position of C-C is at 284.6 eV, and the peak position of C-O and C=O is at 285.6 eV.

In this paper, the degree of graphitization of organic matter is defined as the proportion of the C=C photoelectron spectroscopy peak area. The calculation formula is as follows:

$$\text{Gra.D} = \text{Area}_{\text{C=C}} / (\text{Area}_{\text{C=C}} + \text{Area}_{\text{C-C}} + \text{Area}_{\text{C=O,C-O}}) \quad (2)$$

In the formula, Gra.D represents the degree of graphitization of organic matter, $\text{Area}_{\text{C=C}}$ denotes the peak area of C=C photoelectron spectroscopy, $\text{Area}_{\text{C-C}}$ represents the peak area of C-C photoelectron spectroscopy, and $\text{Area}_{\text{C=O,C-O}}$ indicates the peak area of C=O and C-O photoelectron spectroscopy. Through this method, it is possible to calculate the content or proportion of graphite bonds under different thermal maturity conditions.

3.2.3. Particle Helium Porosity

The porosity of shale, as measured by the particle helium method, is found to be higher than that measured by the plunger helium method and saturated liquid method. This indicates that the particle helium method provides a measurement of the total porosity of shale [40]. To investigate the constraint effect of thermal maturity of organic matter on shale pore development, the variation characteristics of total porosity with thermal maturity can better illustrate this problem. In this paper, the experimental process and conditions of the particle helium method are as follows: ① shale particles are dried at 105 °C for no less than 24 h. ② The sample chamber is vacuumized to 0.1 Pa, then filled with helium at an injection pressure of 1.378 MPa. When the pressure change is less than 0.21 Kpa in 30 min, the helium can be regarded as being at saturated equilibrium. ③ Using Boyle's law and Archimedes' law, the volume of injected helium, the volume of shale rock skeleton, and the total volume of rock are calculated, from which the total porosity of the shale is obtained [40].

3.2.4. CO₂ and N₂ Adsorption

The predominant pores found in the Wufeng–Longmaxi shale within the southern Sichuan Basin are micro-mesopores [21]. Through low-temperature and low-pressure N₂ adsorption experiments, the effective pore size range has been determined to be 2–100 nm. It should be noted that pores with sizes smaller than 2 nm are not measurable in this specific study. The effective pore size range of CO₂, which serves as an adsorbate with high analysis temperature, strong energy, and rapid equilibrium, is determined to be 0.35–2 nm. Therefore, this paper utilizes a combination of these two methods to characterize the microscopic pore structure of shale.

The MicroActive for ASAP 2460 automatic specific surface and pore size analyzer (Micromeritics Instrument Corporation, Norcross, GA, USA) is the instrument employed for both the N₂ adsorption experiment and the CO₂ adsorption experiment. The gas adsorption capacity of shale samples under various pressure conditions is determined using the static volume method of isothermal physical adsorption. The specific method used is as follows: shale samples weighing 3–5 g, with a mesh size of 60–120, were first vacuum degassed at 100 °C for 8 h. Next, an N₂ isothermal adsorption–desorption experiment was conducted in a liquid nitrogen environment (77.4 K). The total pore volume and pore size distribution characteristics were calculated using the BJH (Barrett–Joyner–Halenda) theory and Kelvin equation, respectively. Furthermore, the specific surface area of the shale was determined using the multi-point BET (Brunauer–Emmett–Teller) model. Following the nitrogen adsorption experiment, vacuum degassing was initially carried out, followed by a secondary degassing process lasting 4 h. Subsequently, the CO₂ isothermal adsorption experiment was conducted in an ice water bath (273.1 K). The pore volume and specific surface area of micropores were calculated using the DA (Dubinin–Astakhov) model [41].

3.2.5. SEM

The core samples were cut into 1 cm × 1 cm slices, and the surface of the shale was mechanically smoothed using the German Leica EM TXP automatic target surface processor (Brochure JP, Leica, Wetzlar, Germany). Next, the polished shale flakes were placed into the LJB-1A instrument for argon ion polishing, followed by carbon plating to enhance the shale surface's conductivity. The processed samples were then put into the FEI Helios NanoLab 650 field emission scanning electron microscope (FE-SEM) (FEI Company, Hillsboro, OR, USA). The vacuum was adjusted, the working distance of the electron microscope set to 4 mm, and the surface of the shale observed using the backscattering (CBS) mode.

4. Results

4.1. Laser Raman Maturation of Organic Matter

According to Figure 3 and Table 2, the laser Raman thermal maturity of shale samples related to the Emeishan basalt eruption zone and basement fracture is relatively high,

ranging from 3.54% to 3.72%, with an overall maturity greater than 3.5%. The displacement distance between the D peak and G peak is between 241.76 and 260.82 cm^{-1} , which is less than 261 cm^{-1} . The peak height ratio of the D peak to G peak ranges from 0.73 to 0.83, with an overall ratio greater than 0.70. On the other hand, the laser Raman maturity of shale samples in other stable tectonic areas is low, with values less than 3.6%. The displacement distance between the D peak and the G peak is greater than 261 cm^{-1} , and the peak height ratio of the D peak to G peak is less than 0.7. In summary, as the thermal maturity increases, the displacement spacing between the D peak and G peak gradually decreases, and the peak height ratio between the D peak and G peak gradually increases.

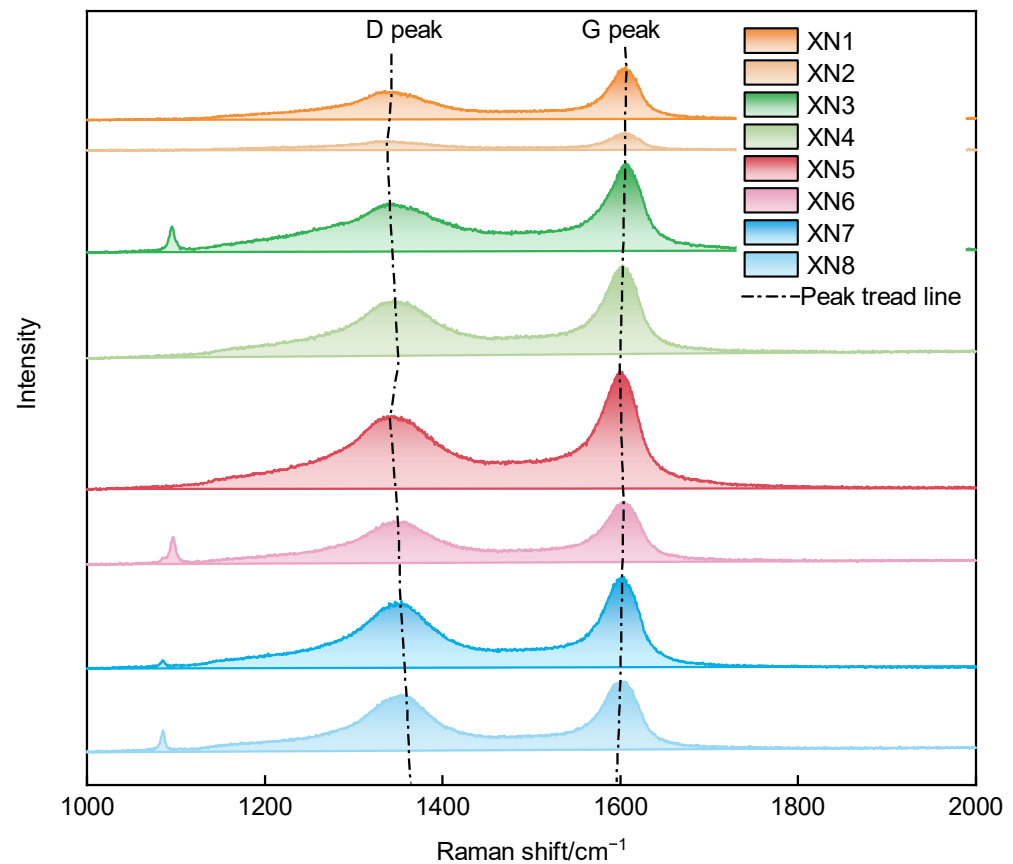


Figure 3. Laser Raman spectroscopy of organic matter.

Table 2. Sample laser Raman parameters.

Sample Number	D-Peak Raman Shift/ cm^{-1}	G-Peak Raman Shift/ cm^{-1}	Distance between D-Peak and G-Peak/ cm^{-1}	D-Peak Raman Intensity	G-Peak Raman Intensity	Ratio between D-Peak Intensity and G-Peak Intensity	Laser Raman Maturation/%
XN1	1335.29	1606.15	270.86	305.37	529.01	0.58	3.43
XN2	1330.53	1604.04	273.51	100.57	181.20	0.56	3.41
XN3	1337.41	1605.63	268.22	543.19	927.62	0.59	3.44
XN4	1344.81	1601.92	257.11	650.43	975.85	0.67	3.54
XN5	1337.94	1599.28	261.34	762.72	1183.42	0.64	3.51
XN6	1344.81	1605.63	260.82	477.05	656.73	0.73	3.61
XN7	1353.81	1604.04	250.23	682.24	908.65	0.75	3.63
XN8	1359.10	1600.86	241.76	601.80	726.48	0.83	3.72

4.2. Graphitization of Organic Matter

According to Figure 4 and Table 3, the photoelectron spectroscopy characteristics of the organic matter in eight samples are similar, and the peak intensity of C=C, C-C, and C-O/C=O can be determined using peak fitting techniques. The peak fitting results reveal that the peak area of C-C remains relatively constant, while the peak area of organic matter C-O/C=O in shale near the Emeishan basalt eruption zone and basement fault is relatively small, and the peak area of C=C is relatively large. This suggests that the decrease in C=O/C-O in organic matter is the cause of the increase in C=C in the thermal anomaly area. This can be explained by the chemical principle that lower energy levels correspond to greater stability. The functional group bond energy of C=O/C-O is 285.6 eV (maximum), while the functional group bond energy of C=C is 284.3 eV (minimum). To maintain the structural stability of organic matter, the C=O/C-O bonds are converted to C=C.

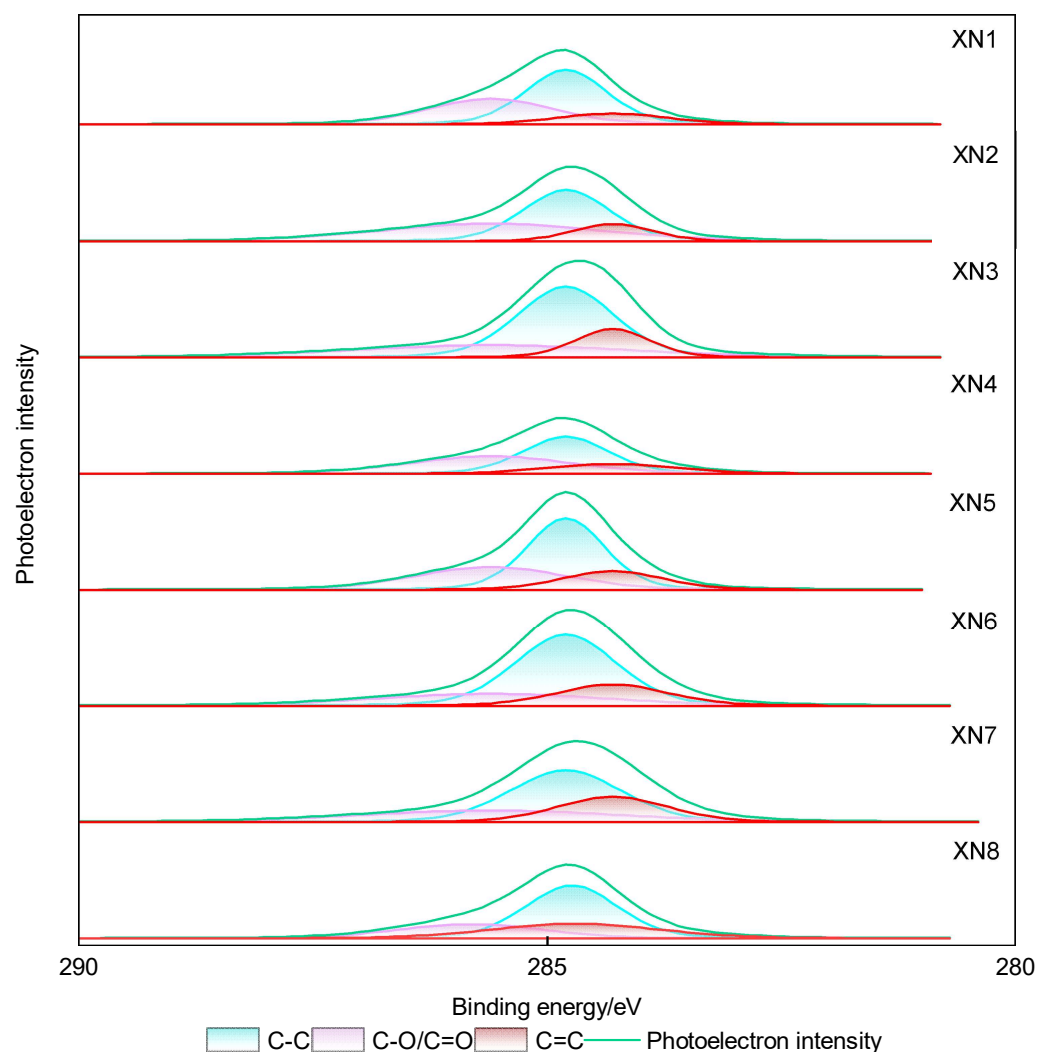


Figure 4. XPS peak fitting results.

Based on the above analysis and Table 3, the graphitization degree of organic matter in the wide and gentle structure is low, ranging from 13.83% to 17.51%. In contrast, the organic matter in the shale near the Emeishan basalt eruption zone and the basement fault maintains structural stability by having a higher number of C=C bonds, resulting in a higher graphitization degree ranging from 19.13% to 26.19%.

4.3. Porosity of Shale

According to Figure 5, the porosity of XN1 and XN2 is between 3% and 4%. The porosity of XN3 and XN4 is between 5% and 6%, which is 1.45% to 2.34% higher than that of the first two samples. The porosity of XN5 is 7.76%, which is 2.67% and 1.85% higher than that of XN3 and XN4, respectively. The porosity of XN6, XN7, and XN8 is lower than that of the first five samples. The porosity of XN6 is 2.92%, which is 4.84% lower than that of XN5. The porosity of XN7 and XN8 is basically 1.5%, approximately 1.4% lower than that of XN6. From the data distribution in Figure 4, it can be observed that the shale porosity shows a trend of slow rise, rapid rise, slow rise, rapid rise, rapid decline, rapid decline, and stable low values from XN1 to XN8.

Table 3. Samples of photoelectronic parameters of carbon-containing functional groups and the degree of organic matter graphitization.

Sample Number	Photoelectron Intensity Area of C=C	Photoelectron Intensity Area of C-C	Photoelectron Intensity Area of C=O/C-O	Photoelectron Intensity Area of Carbon-Containing Functional Groups	Graphitization Degree/%
XN1	2461.56	8931.32	6402.91	17,795.79	13.83
XN2	2770.28	8983.83	7876.51	19,630.62	14.11
XN3	4265.97	13,749.98	6913.97	24,929.92	17.11
XN4	2515.45	6421.52	5725.95	14,662.92	17.16
XN5	3873.58	11,245.62	7003.38	22,122.57	17.51
XN6	4834.36	14,683.32	5747.67	25,265.35	19.13
XN7	5712.12	11,729.95	6181.73	23,623.80	24.18
XN8	5004.90	9876.92	4227.84	19,109.66	26.19

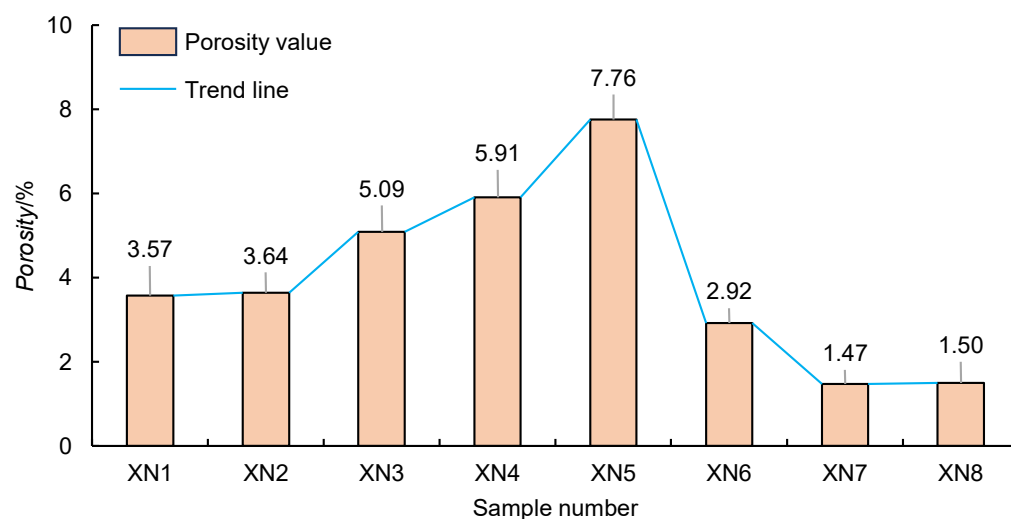


Figure 5. Porosity distribution histogram.

4.4. Pore Structure of Shale

4.4.1. CO₂ and N₂ Adsorption Isotherms

According to Figure 6a, the CO₂ adsorption capacity of all the samples increases rapidly when the relative pressure is less than 0.005. However, when the relative pressure exceeds 0.005, the increase in CO₂ adsorption capacity becomes slower. In the relative pressure range of 0 to 0.03, the difference between the CO₂ adsorption curve and the desorption curve for each sample is relatively consistent. To facilitate a better comparison of the pore structure in the 0 to 2 nm pore size range, the experimental results were processed using the DA (Dubinin–Astakhov) model. The processing results and analysis can be found in Section 4.4.2.

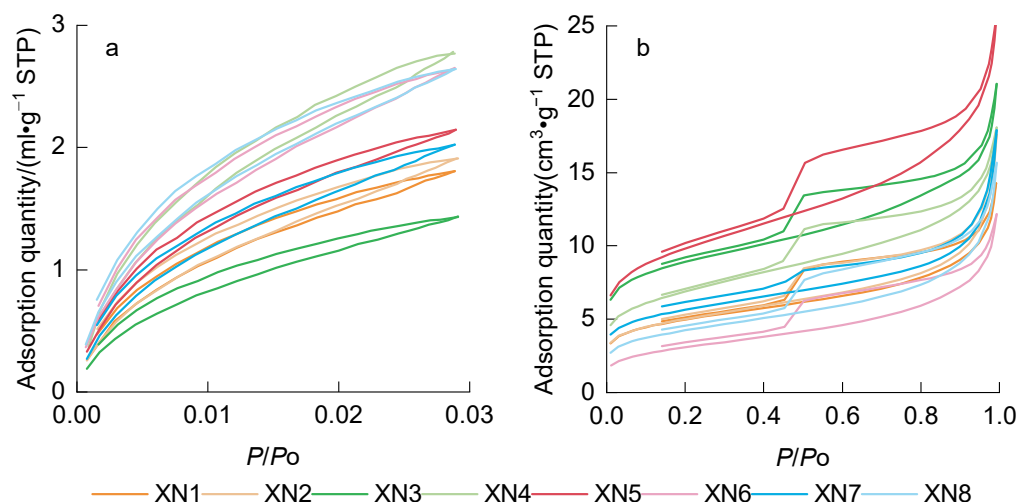


Figure 6. Adsorption isotherms. (a) CO₂ adsorption isotherm; (b) N₂ adsorption isotherm.

According to Figure 6b, there is an inflection point in the N₂ desorption curve of each sample at a relative pressure of 0.45. The adsorption isotherms of all the samples conform to the Type IV classification as per the IUPAC adsorption isotherm standard. Additionally, the hysteresis loop of the XN1–XN5 samples is larger compared to the XN6, XN7, and XN8 samples, indicating the development of ink bottle pores in the XN1–XN5 samples and parallel plate pores in the XN6–XN8 samples. Figure 6b also indicates that the adsorption capacity of the XN1–XN5 samples generally exhibits a gradual increasing trend, while XN6 shows a sharp decrease in adsorption capacity, and XN6 is similar to XN7 and XN8 in terms of adsorption capacity. Finally, for a more detailed analysis of pore structures within the pore size range of 2 to 100 nm, please refer to Section 4.4.3.

4.4.2. The 0–2 nm Pore Structure

Based on Figure 7, the pore structure of each sample can be divided into three parts when the pore size is less than 1 nm: the part between the left peak trend line and the center front trend line, the part between the center front trend line and the right peak trend line, and the portion to the right of the right peak trend line.

Between the left peak trend line and the center front trend line, each sample exhibited three peaks, except for the XN7 sample, which showed four peaks. The pore structure parameters of each sample are presented in Table 4. Except for XN7, the pore volume and specific surface area of the two peaks on the left (XN1–XN8) generally showed an initial increase followed by a decrease. As for the third peak, the pore volume and specific surface area did not exhibit a clear pattern of change. While the pore volume and specific surface area of the four peaks in the XN7 sample are larger, the width of each peak is relatively small, and the peak area is essentially similar to that of the adjacent two samples. Based on the distance between the left peak trend line and the center front trend line, the XN1–XN3 samples had a small and relatively constant distance, while the distance between the XN3–XN5 samples gradually increased and then stabilized (Figure 7).

Table 4. Pore structure parameters between left peak trend line and center front trend line.

Sample Number	Pore Diameter /nm	Pore Volume /(mL·g ^{−1} ·nm ^{−1})	SSA /(m ² ·g ^{−1} ·nm ^{−1})	Sample Number	Pore Diameter /nm	Pore Volume /(mL·g ^{−1} ·nm ^{−1})	SSA /(m ² ·g ^{−1} ·nm ^{−1})
XN1	0.5416	0.0248	112.033	XN5	0.5241	0.031	140.295
	0.594	0.0174	78.801		0.594	0.0213	96.457
	0.6464	0.0121	54.733		0.6464	0.0205	93.089

Table 4. Cont.

Sample Number	Pore Diameter /nm	Pore Volume /(mL·g ⁻¹ ·nm ⁻¹)	SSA /(m ² ·g ⁻¹ ·nm ⁻¹)	Sample Number	Pore Diameter /nm	Pore Volume /(mL·g ⁻¹ ·nm ⁻¹)	SSA /(m ² ·g ⁻¹ ·nm ⁻¹)
XN2	0.5416	0.0285	128.83	XN6	0.5241	0.022	99.607
	0.594	0.0221	100.268		0.594	0.0138	62.693
	0.6464	0.0079	35.605		0.6464	0.0118	53.499
XN3	0.5416	0.0369	167.1	XN7	0.5241	0.0397	179.619
	0.594	0.0296	134.241		0.559	0.0287	130.538
	0.6464	0.0205	92.896		0.594	0.0267	120.943
XN4	0.5416	0.0305	138.021	XN8	0.6464	0.0193	87.334
	0.594	0.0204	92.184		0.5241	0.0191	86.284
	0.6464	0.0159	72.292		0.5765	0.0134	60.885
					0.6464	0.0126	57.216

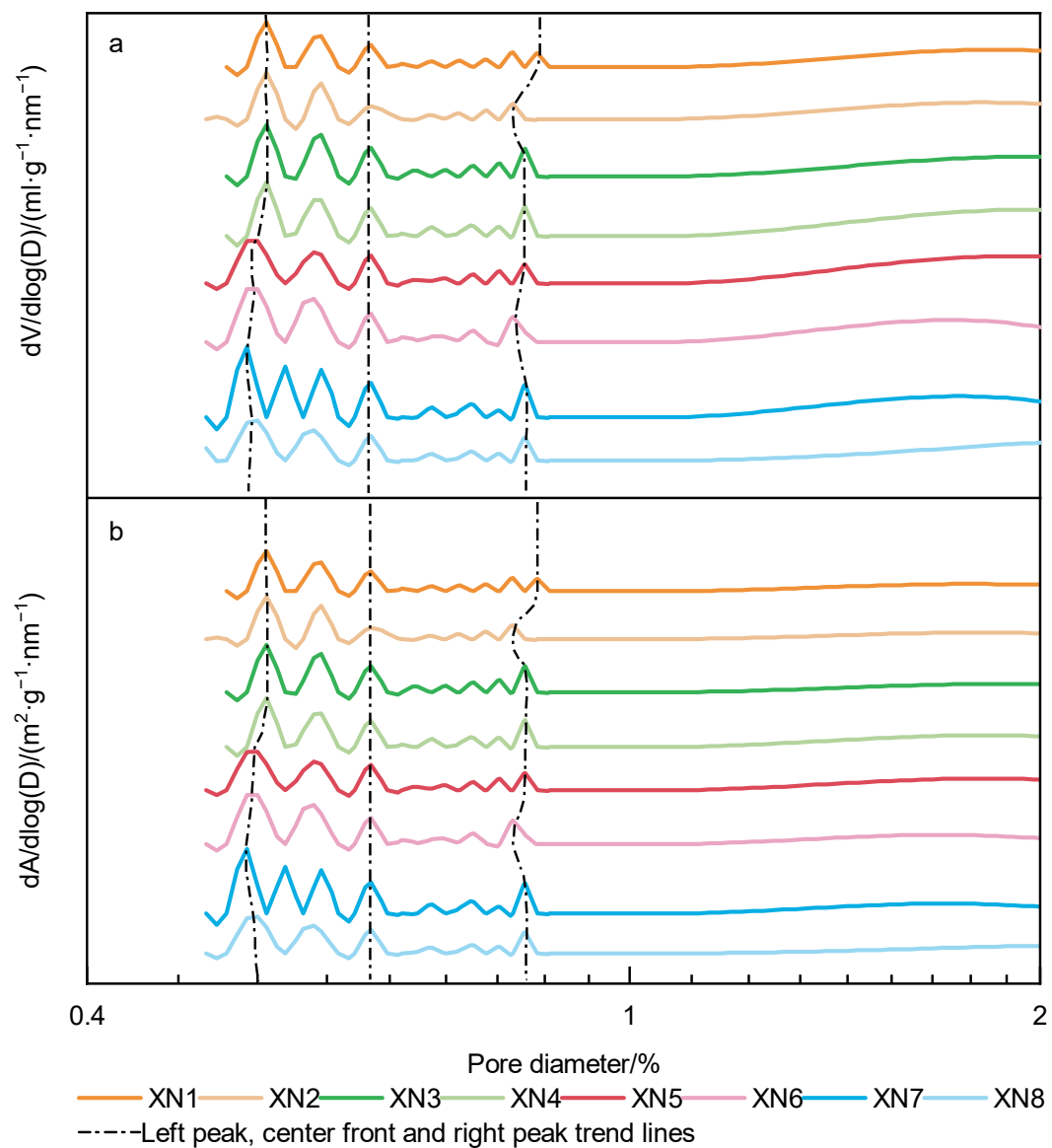


Figure 7. The 0–2 nm pore structure characteristics. (a) Pore volume differential distribution versus pore diameter (D); (b) pore-specific surface area (SSA) differential distribution versus pore diameter (D).

The change trend in pore volume and specific surface area of each sample between the center front trend line and the right peak trend line is essentially consistent with that between the left peak trend line and the center front trend line. The value peaks in the XN3 sample, followed by a decrease (except for the XN7 sample). Figure 7 illustrates that the distance between the center front trend line and the right peak trend line does not display a clear pattern.

In the right section of the right peak trend line, the pore volume and specific surface area of XN1–XN5 exhibited an increasing trend, while the pore volume and specific surface area of XN5–XN8 demonstrated a decreasing trend (Figure 7).

4.4.3. The 2–100 nm Pore Structure

In the 2–15 nm range, the pore volume and specific surface area of XN1–XN5 exhibited a gradual increase. The pore volume and specific surface area of the XN6 sample experienced a sudden drop compared to XN5, while those of XN6, XN7, and XN8 were essentially the same. The pore volume was approximately $0.01 \text{ mL} \cdot \text{g}^{-1} \cdot \text{nm}^{-1}$ in each pore size range, and the specific surface area was around $10 \text{ m}^2 \cdot \text{g}^{-1} \cdot \text{nm}^{-1}$ in each pore size range (Figure 8).

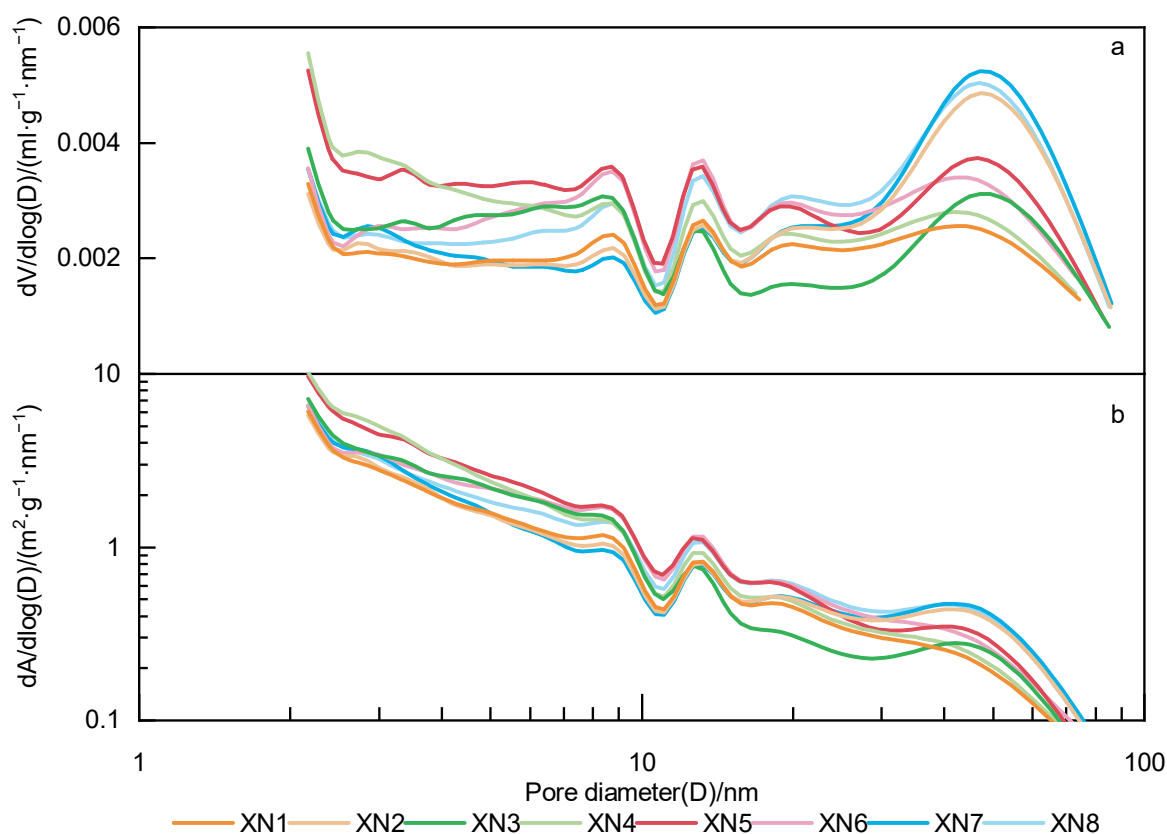


Figure 8. The 2–100 nm pore structure characteristics. (a) Pore volume differential distribution versus pore diameter (D); (b) pore-specific surface area (SSA) differential distribution versus pore diameter (D).

The pore size ranges from 15 to 35 nm. Apart from XN5, which has a pore volume greater than $0.15 \text{ mL} \cdot \text{g}^{-1} \cdot \text{nm}^{-1}$, the pore volume of the other samples is approximately $0.10 \text{ mL} \cdot \text{g}^{-1} \cdot \text{nm}^{-1}$ (Figure 8a). The change trend in specific surface area and pore volume is consistent. Additionally, the specific surface area of XN5 is $1\text{--}2 \text{ m}^2 \cdot \text{g}^{-1} \cdot \text{nm}^{-1}$ larger than that of the other samples (Figure 8b).

In the 35–100 nm pore size range, the pore volume of XN1, XN4, and XN6 is consistently below $0.01 \text{ mL} \cdot \text{g}^{-1} \cdot \text{nm}^{-1}$, with no significant difference. The specific surface area

is also below $2 \text{ m}^2 \cdot \text{g}^{-1} \cdot \text{nm}^{-1}$. XN2 and XN7 exhibit similar pore volumes, reaching a maximum value of $0.023 \text{ mL} \cdot \text{g}^{-1} \cdot \text{nm}^{-1}$. XN5 has the second highest pore volume, with a maximum value of $0.02 \text{ mL} \cdot \text{g}^{-1} \cdot \text{nm}^{-1}$. The pore volume of XN8 is $0.18 \text{ mL} \cdot \text{g}^{-1} \cdot \text{nm}^{-1}$, which is smaller than that of XN5. XN3 has a smaller pore volume of $0.15 \text{ mL} \cdot \text{g}^{-1} \cdot \text{nm}^{-1}$ compared to XN5. Due to the wide range of pore sizes, there is little difference in the specific surface area of XN2, XN3, XN5, XN7, and XN8, but it is larger than that of XN1, XN4, and XN6 (Figure 8).

4.4.4. The 0–100 nm Pore Structure

The accuracy of the differential change in pore volume and specific surface area with pore size is influenced by the number of data points in the fitting model. When there are fewer data points, the differential change in pore volume and specific surface area with pore size becomes less accurate. In comparison, the cumulative distribution of pore volume and specific surface area with pore size is more accurate than the differential distribution because it is based on the cumulative total pore volume measured through experiments.

From Figure 9a, it is evident that there is no significant difference in the cumulative pore volume of the eight shale samples within the range of 0 to 2 nm. Notably, the pore volume of XN1 and XN6 consistently remains the smallest between 2 and 15 nm, while the pore volume of XN5 consistently remains the largest. The pore volume growth rate of XN2, XN7, and XN8 is consistent, whereas the pore volume of the XN3 and XN4 samples exhibits a rapid increase. Furthermore, the pore volume of the XN5 sample remains the largest between 15 and 100 nm, with a final cumulative pore volume of $0.035 \text{ mL} \cdot \text{g}^{-1}$. Following closely are the pore volumes of XN2, XN3, XN4, and XN7, ranging between 0.025 and $0.027 \text{ mL} \cdot \text{g}^{-1}$ in terms of final cumulative pore volume. The cumulative pore volume of the XN8 sample is recorded at $0.0225 \text{ mL} \cdot \text{g}^{-1}$, while the cumulative pore volume of XN1 and XN6 remains the smallest at $0.018 \text{ mL} \cdot \text{g}^{-1}$.

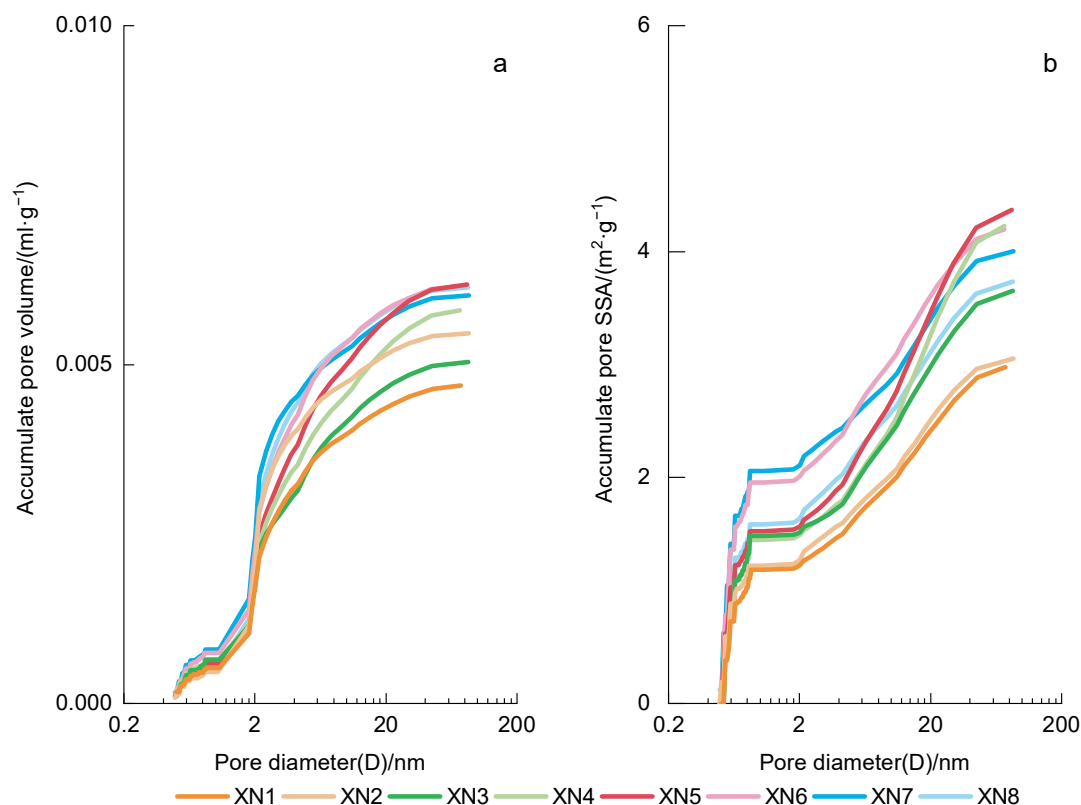


Figure 9. The 0–100 nm pore structure characteristics. (a) Accumulated pore volume versus pore diameter (D); (b) accumulated pore-specific surface area (SSA) versus pore diameter (D).

From Figure 9b, it is evident that the cumulative specific surface area of XN3, XN5, and XN7 is the largest within the range of 0 to 2 nm, with a maximum value of 7 to 9 m²·g^{−1}. Following closely, the cumulative specific surface area of XN2, XN4, XN6, and XN8 ranks second, reaching a maximum value of 5.5 to 6 m²·g^{−1}. Meanwhile, XN1 exhibits the smallest cumulative specific surface area, with a maximum value of 5 m²·g^{−1}. Moving to the range of 2 to 100 nm, XN5 consistently maintains the maximum cumulative specific surface area, reaching a remarkable maximum value of 25 m²·g^{−1}. Additionally, the cumulative specific surface area of XN3, XN4, and XN7 follows, ranging between 16 and 19 m²·g^{−1}, with XN3 and XN4 exhibiting a greater growth rate compared to XN7. On the other hand, the cumulative specific surface area of XN1, XN2, XN6, and XN8 remains the smallest, with maximum values ranging between 11 and 14 m²·g^{−1}.

5. Discussion

5.1. Relationship between Graphitization and Laser Raman Maturation

The thermal evolution process of organic matter governs both the thermal maturity and the composition of organic functional groups, and these two factors exhibit a corresponding relationship. During the early stages of thermal maturity ($R_o < 0.5\%$), the organic matter undergoes deoxidation, leading to the removal of oxygen-containing functional groups. During the mature stage of thermal evolution (R_o between 0.5% and 1.3%), the organic matter undergoes further decomposition, resulting in the generation of a significant quantity of crude oil. This crude oil primarily consists of chain-like carbon-containing organic polymers. In the high-maturity stage ($R_o = 1.3\%–2.0\%$), the crude oil undergoes cracking, resulting in the separation of the low-carbon group from the original polymer in the branched chain. In the over-maturity stage ($R_o > 2.0\%$), there is an increase in aromatization and graphitization of organic matter. As thermal maturity increases, the chemical reaction proceeds more extensively, leading to an increase in the content of graphite bonds (C=C) [42]. Based on the aforementioned principle, when R_o is less than 2.0%, the degree of graphitization of organic matter remains largely unchanged with increased thermal maturity. However, when R_o exceeds 2.0%, the degree of graphitization of organic matter tends to gradually increase as the thermal maturity progresses.

The Wufeng–Longmaxi shales found in the Sichuan Basin are characterized as being in the over-mature stage [43]. Figure 10 illustrates a clear positive correlation between the graphitization degree of organic matter in shale and the laser Raman thermal maturity of organic matter, with a correlation coefficient of 0.85. This indicates that the graphitization degree of organic matter can be determined using the fitting relationship presented in Figure 10 and the thermal maturity measured through experiments. This approach enables the effective evaluation of the gas generation capacity of organic matter under various thermal maturity conditions. Such evaluations hold great significance in optimizing favorable exploration areas for shale gas.

5.2. Control of Shale Porosity by Thermal Evolution

The thermal maturity of organic matter in the Wufeng Formation–Longmaxi Formation shale in the southern Sichuan Basin is typically less than 3.5%. Conversely, the thermal maturity of the Changning Shuanglong–Luochang syncline and Jianwu syncline near the Huayingshan basement fault zone and the Emeishan basalt eruption zone, as well as the Luzhou Yunjin syncline near the basement fault zone and distant from the Emeishan basalt eruption zone, exceeds 3.5% [43]. Based on the thermal simulation results of low-maturity organic matter, the yield of methane demonstrates an increasing trend when R_o (reflectance of organic matter) is below 3.6%. At an R_o value of 3.6%, the yield of methane reaches its peak. However, when R_o exceeds 4.3%, the yield of methane is lower compared to when R_o is at 3.0% [44]. This phenomenon is likely linked to the increase in thermal maturity and the capacity of organic matter to generate methane.

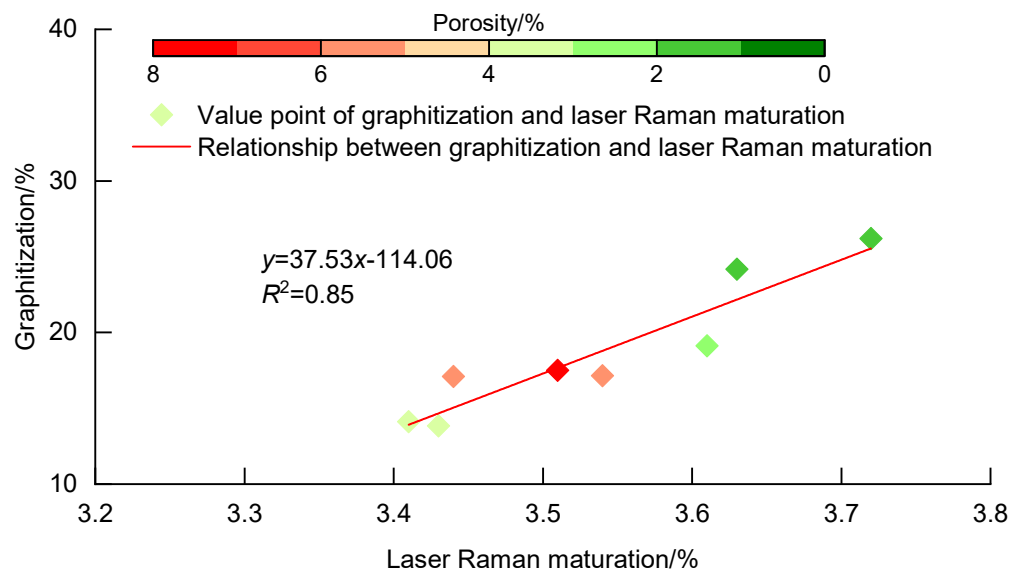


Figure 10. Relationship between graphitization and laser Raman maturation.

Based on the findings presented in Figure 10, it has been observed that, when the thermal maturity of shale, represented by R_o , is below 3.6%, there is a gradual increase in shale porosity. This increase in porosity can be attributed to the cracking of organic matter, which generates methane, as well as the resulting pressurization from hydrocarbon generation. Based on the information provided, the thermal maturity of the Wufeng Formation–Longmaxi Formation shale in southern Sichuan is exceptionally high only near the basement fault zone, where R_o exceeds 3.6%. However, based on the relationship between methane yield and thermal maturity, the thermal maturity of XN1–XN8 is below 4.3%, indicating that they all possess good methane production capacity. This suggests that continuous hydrocarbon generation pressurization does not contribute to the increase in shale porosity. The most plausible explanation for these observations is an abnormal thermal event caused by heat transfer in the basement fault. The presence of the basement fault results in worsened shale gas preservation conditions. Consequently, shale gas is lost, and the formation pressure of shale gas reservoirs is unable to counterbalance the surrounding compressive stress, leading to a decrease in shale porosity.

5.3. Control of Shale Pore Structure by Thermal Evolution

The analysis of the pore volume and specific surface area distribution with respect to pore size reveals that, within the pore size range of 0 to 15 nm, both the pore volume and specific surface area initially increase and then decrease with rising thermal maturity. Due to the fact that the differential distribution of pore volume and specific surface area is reliant on the fitting accuracy of the adsorption model and the number of fitting points, the cumulative distribution of pore volume and specific surface area, which is acquired through experimental means, evidently offers a higher level of accuracy in characterizing the pore structure compared to the differential distribution. According to the data presented in Figure 9, it can be observed that, within the pore size range of 15 to 100 nm, the pore volume and specific surface area likewise exhibit a pattern of initially increasing and then decreasing with increasing thermal maturity. The anomalous behavior observed in the XN6 sample may be attributed to its low TOC. If the TOC is adjusted to match that of the other samples, the cumulative distribution of pore volume and specific surface area would be substantially similar to that of the XN7 sample.

Physical quantities such as pore volume and specific surface area can only partially capture the pore structure of shale, and they are unable to fully depict the pore count and morphology. As crucial structural parameters, the number and morphology of pores offer a more comprehensive reflection of the mechanism behind changes in pore structure. Consid-

ering the significant burial depth, strong compaction, and mosaic contact between particles in the Wufeng Formation–Longmaxi Formation shale in southern Sichuan, the single-hole features of the shale can be elucidated using the cylindrical model. The calculation formula for pore volume and surface area under a certain pore diameter is as follows:

$$\begin{cases} V = N \cdot \frac{\pi \cdot D^2 \cdot H}{4} \\ SA = N \cdot \pi \cdot D \cdot \left(\frac{D}{2} + H \right) \end{cases} \quad (3)$$

In the formula, V represents the pore volume of all the apertures, measured in nm^3 ; N stands for the number of all apertures, dimensionless; π denotes the circumference ratio, which is approximately 3.14; D represents the aperture, measured in nm ; H signifies the average length of the pores, measured in nm ; SA represents the surface area of all pores under a certain pore size, measured in nm^2 .

The relationship between the average pore length (H) and the pore size (D) can be determined by solving Formula (3), as follows:

$$H = \frac{2 \cdot \frac{V}{SA} \cdot D}{D - 4 \cdot \frac{V}{SA}} \quad (4)$$

The ratio of pore volume (V) to surface area (SA) of all pores under a certain pore size can also be expressed by the following formula:

$$\frac{V}{SA} = \frac{V_1 - V_2}{SA_1 - SA_2} = \frac{\frac{V_1 - V_2}{D_1 - D_2}}{\frac{SA_1 - SA_2}{D_1 - D_2}} = \frac{dF_V(D)}{dF_{SA}(D)} \quad (5)$$

In the formula, V_1 represents the cumulative pore volume of the previous pore size, measured in nm^3 ; V_2 represents the cumulative pore volume of this pore size, measured in nm^3 ; D_1 represents the previous aperture, measured in nm ; D_2 represents the pore size, measured in nm ; SA_1 represents the cumulative surface area of the previous pore size, measured in nm^2 ; SA_2 represents the cumulative surface area of the pore size, measured in nm^2 ; $dF_V(D)$ represents the slope of the cumulative distribution function of pore volume under this pore size, measured in nm^2 ; $dF_{SA}(D)$ represents the slope of the cumulative distribution function of the surface area under this pore size, measured in nm .

The results are presented in Figures 11 and 12. Based on Figure 11, all the samples exhibit the characteristic of a gradual decrease in the number of pores with an increase in pore size. As for Figure 12, it shows that, when the pore size is less than 2 nm, the ratio of pore size to pore extension length demonstrates a decreasing trend, while, for pore sizes greater than 2 nm, the ratio of the two shows an increasing trend.

When the pore size is less than 2 nm (micropore), the number of pores increases with the rise in thermal maturity (as observed in Table 2, where the thermal maturity of XN1–XN8 generally demonstrates increasing characteristics). At an R_o value of 3.5% or when the degree of graphitization of organic matter reaches 17%, the number of pores reaches its maximum. When R_o exceeds 3.5% or the degree of graphitization of organic matter surpasses 17%, the number of pores exhibits a gradual decrease, as illustrated in Figure 11. The high number of pores in XN7 could be attributed to its higher TOC compared to XN6 and XN8. As thermal maturity increases, the ratio of pore size to pore extension length gradually rises, with the exception of XN1 and XN6, as depicted in Figure 12. For XN6, with a TOC of only 3.1%, increasing its TOC to the same level as that of XN7 and XN8 could result in a 20% to 40% increase in the ratio of pore size to pore length, bringing the corrected ratio to a level similar to that of XN7 and XN8. For XN1, the ratio of pore size to pore length is 1.5 times greater than that of the other samples (with the ratio curves of the other samples being more concentrated). When the pore size exceeds 2 nm, the ratio of pore size to pore length for the XN1 sample is significantly smaller than that of the other samples, potentially indicating the presence of cracks within the sample (Figure 13a,b).

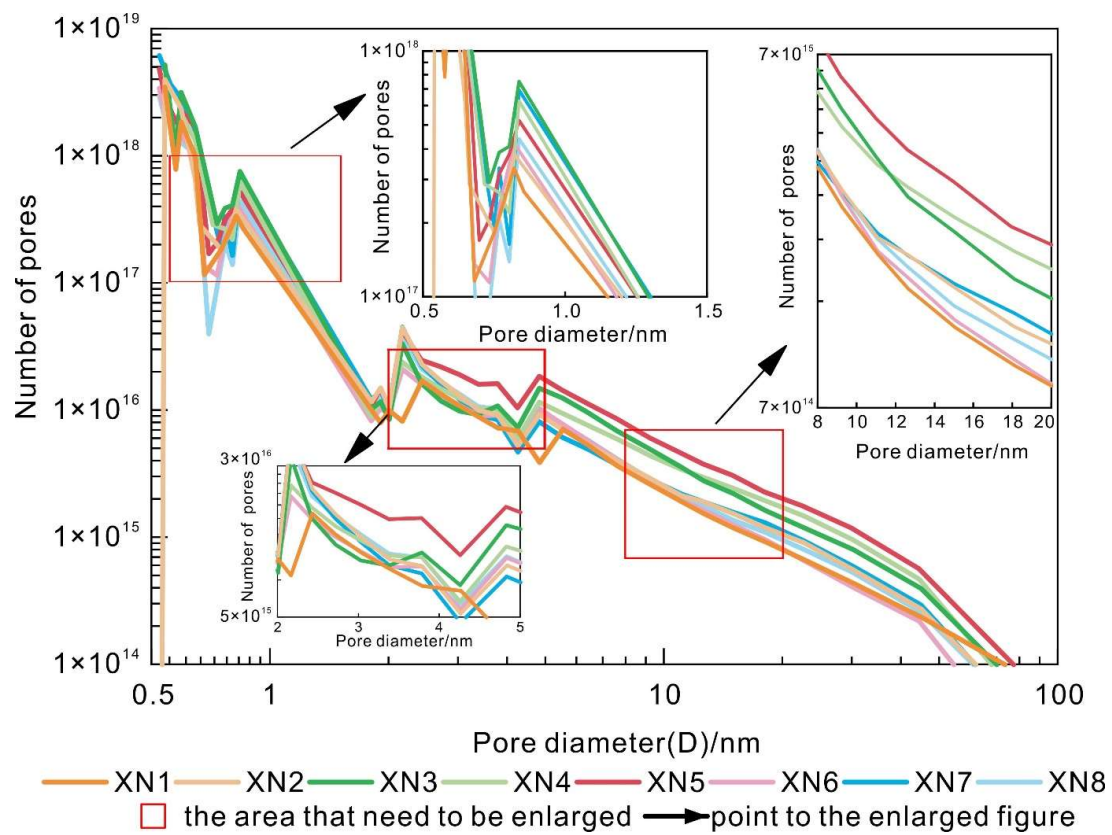


Figure 11. Relationship between number of pores and pore diameter.

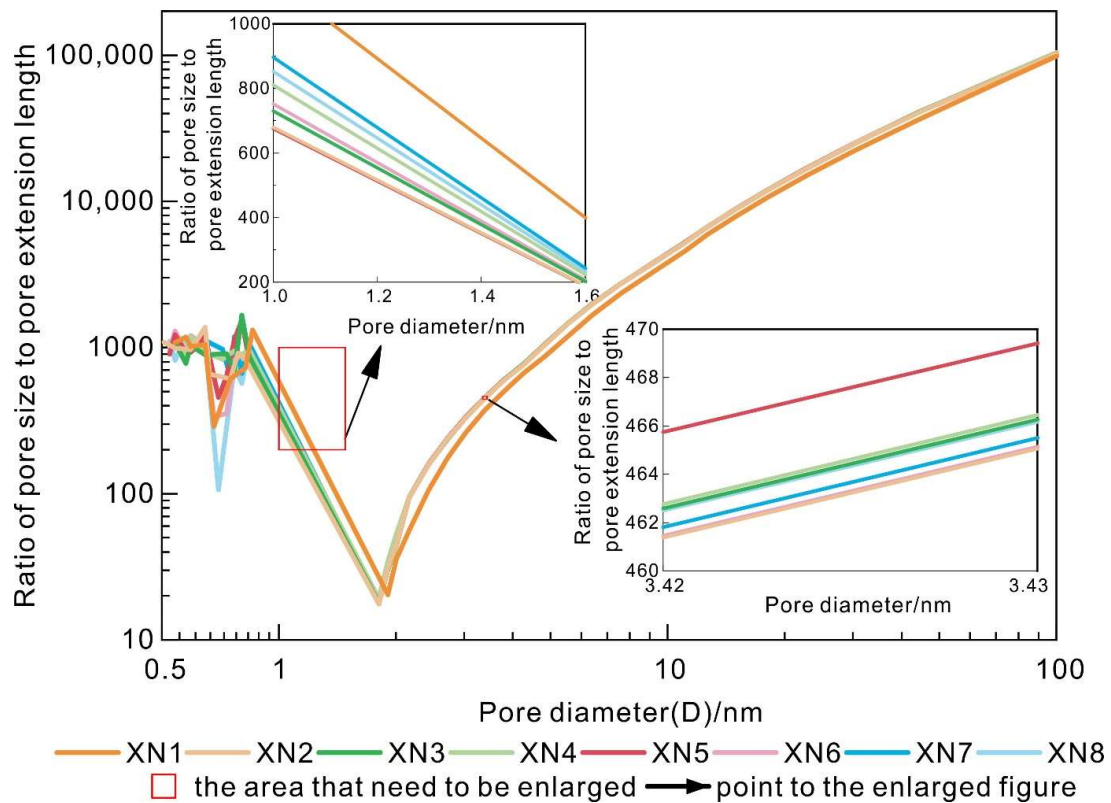


Figure 12. Relationship between ratio of pore size to pore extension length and pore diameter.

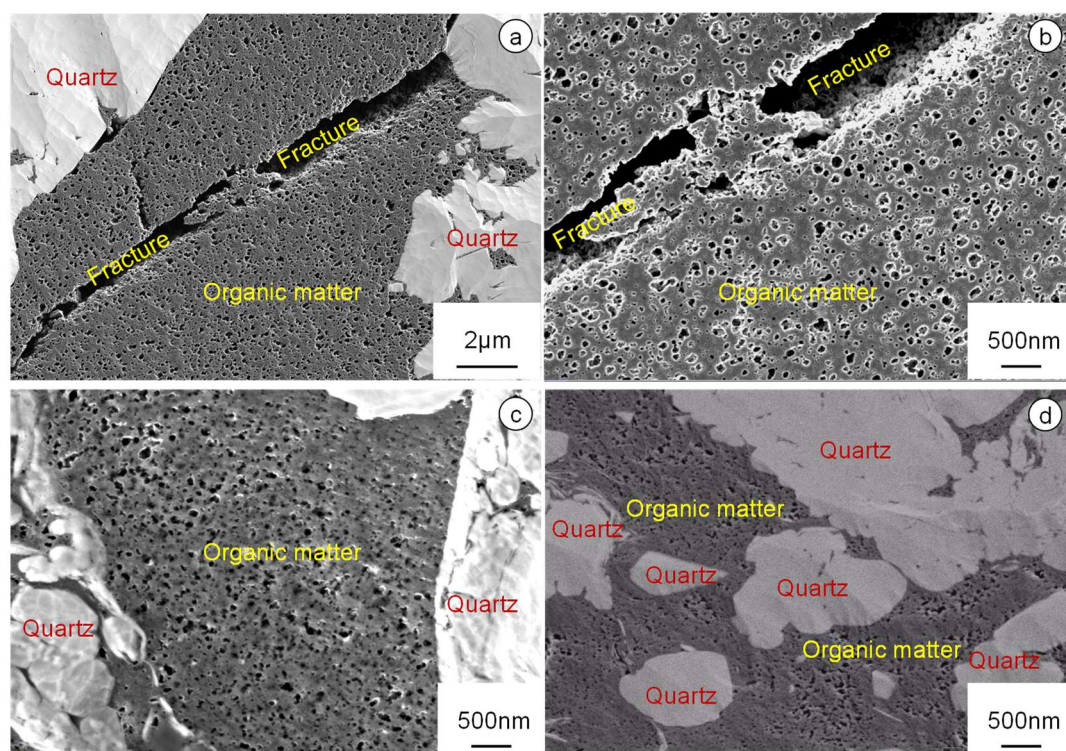


Figure 13. Microscopic characteristics of typical samples. (a) XN1, 4315 m, $R_o = 3.43\%$, graphitization degree = 13.83, 2 μm . (b) XN1, 4315 m, $R_o = 3.43\%$, graphitization degree = 13.83, 500 nm. (c) XN5, 4125 m, $R_o = 3.51\%$, graphitization degree = 17.51%, 500 nm. (d) XN7, $R_o = 3.63\%$, graphitization degree = 24.18%, 500 nm.

When considering the mesopores with pore diameters ranging from 2 to 50 nm, the number of pores and the ratio of pore diameter to pore length exhibit an initial increase followed by a decrease as thermal maturity increases. The peak value occurs at $R_o = 3.5\%$ (where the degree of graphitization of organic matter reaches 17%). When considering macropores with pore sizes greater than 50 nm, the change in the number of pores and the ratio of pore size to pore length with thermal maturity are similar to those observed in the range of 2 to 50 nm. However, for the XN6–XN8 samples, the number of pores decreases sharply and reaches the lowest value among all the samples. Similarly, the ratio of pore size to pore length for the XN6–XN8 samples is also among the lowest values compared to the other samples (Figures 11–13).

Based on the above analysis and the hydrocarbon generation process of organic matter, it can be concluded that, as thermal maturity increases, crude oil begins to undergo cracking, leading to the generation of pores, while organic pores begin to develop from the beginning. According to this idea, it can be inferred that, as thermal maturity increases, the branch chains in crude oil start to detach, forming micropores. As the number of micropores increases, they may interconnect, thereby lengthening the overall extension of the micropores while reducing the overall number of pores. Concurrently, the branched chains near the micropores can continue to detach, potentially transforming into mesopores. In this manner, the current pore structure is ultimately formed (Figure 13).

Based on the geological background, the high thermal maturity of XN6–XN8 is influenced by abnormal thermal events, which in turn are impacted by basement faults, leading to poor preservation conditions for shale gas. When the pore size exceeds 5 nm, the ratio of pore size to pore extension length is higher than that of micropores (pore size less than 2 nm), indicating a greater likelihood of pore connectivity. Additionally, as the pore size increases, the probability of pore connectivity also increases. In this case, shale gas within pores larger than 5 nm will escape through interconnected pores and fractures near the

fracture zone, causing the collapse of those pores. Conversely, the shale gas contained within the micropores (pores with a size less than 2 nm) remains preserved due to the limited connectivity of these pores and their shorter extension length. However, as thermal maturity increases, the branch chain of organic matter continues to break away, leading to the connection of some micropores. This process ultimately results in a decrease in the number of micropores while simultaneously increasing the ratio of pore size to pore extension length (Figures 11 and 12).

5.4. Patterns of Shale Pore Structure Development Controlled by Thermal Evolution

Previous studies have indicated that the pores within the shale of the Wufeng Formation–Longmaxi Formation in the southern Sichuan Basin are primarily attributed to organic matter pores [23]. Considering the geological conditions and the complete process of hydrocarbon generation and organic matter evolution in the Wufeng Formation–Longmaxi Formation, the evolution of pore structure in shale (organic matter) during the over-mature stage ($R_o > 2.0\%$) can be categorized into two stages.

In the first stage (R_o : 2.0%–3.5% or the degree of graphitization of organic matter: 0%–17%), crude oil or asphalt undergoes cracking, causing the detachment of branched chains and the formation of micropores (pore size less than 2 nm). As thermal maturity increases, the branch chains near the micropores continue to detach and form meso-macropores (pore size larger than 2 nm). The detachment of these branch chains enhances the connectivity of micropores, mesopores, and macropores, resulting in improved pore connectivity. Furthermore, the larger the pore size, the better the connectivity between the pores. In this process, the porosity of shale gradually increases (Figure 14).

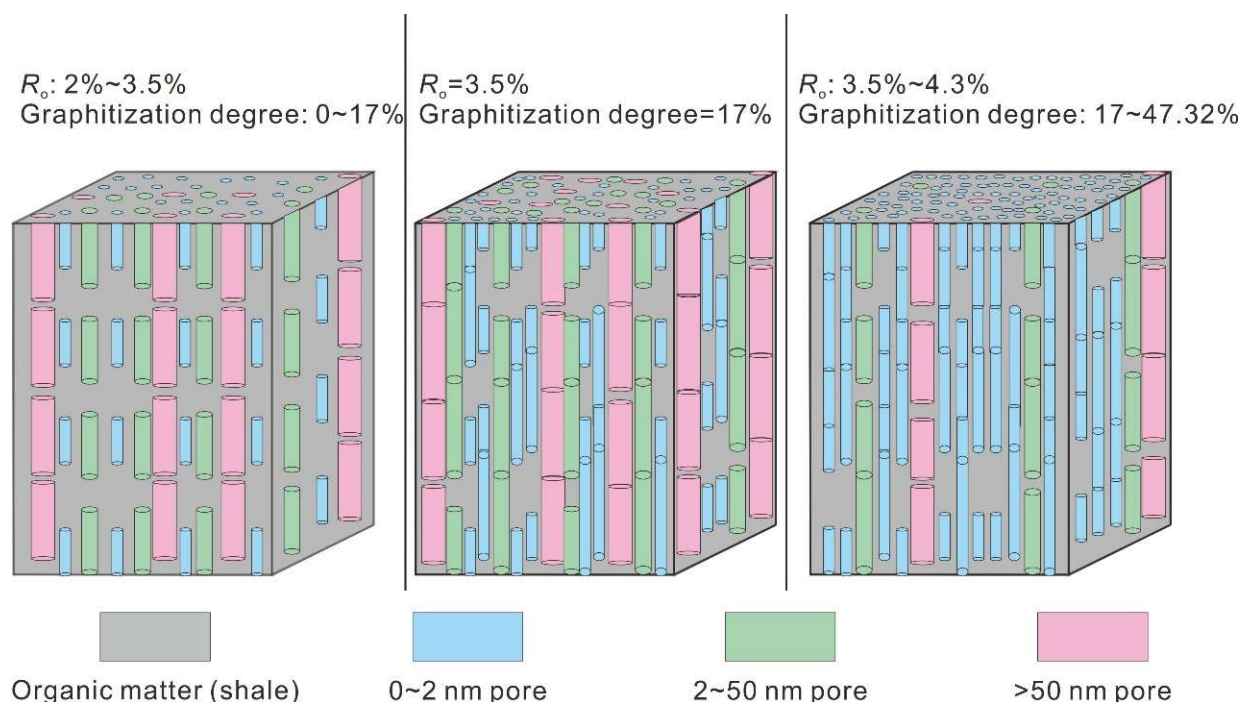


Figure 14. The evolution diagram of small pores, mesopores, macropores, and connectivity in shale with the increase in thermal maturity.

In the second stage (R_o : 3.5%–4.3% or graphitization degree of organic matter: 17%–47.32%), as thermal maturity increases, the branches in the functional groups continue to fall off, leading to the continued generation of micropores (pore size less than 2 nm). The increased number of micropores serves to connect the originally isolated micropores, thus improving the overall connectivity of micropores. However, after the connection merges, the number of micropores begins to show a decreasing trend. The exceptionally

high maturity of this stage is controlled by the basement faults, leading to worsening preservation conditions. Under the influence of the fracture network, shale gas in the medium macropores (pore size greater than 2 nm, with good connectivity) is lost, and the pore collapse becomes smaller or even disappears (the magnitude and degree of macropore collapse are greater than those of mesopores). Throughout this process, the porosity of shale tends to gradually decrease (Figure 14).

6. Conclusions

In this paper, we have analyzed the relationship between porosity, pore structure, laser Raman thermal maturity, and the graphitization degree of organic matter. We thus draw the following conclusions:

- (1) The degree of graphitization of organic matter is a microscopic manifestation of thermal maturity, and there is a significant positive correlation between them, with a correlation coefficient of 0.85 for the fitting equation.
- (2) With the increase in thermal maturity, the porosity, pore volume, and specific surface area of shale initially increase and then decrease. The corresponding thermal maturity at the peak is 3.5% (with a graphitization degree of organic matter at 17%).
- (3) The thermal maturity ranges from 2.0% to 3.5% (with an organic matter graphitization degree of 0% to 17%). During this stage, the branched chains on crude oil or asphalt detach, leading to the formation of micropores with a pore size less than 2 nm. As the thermal maturity increases, the number of micropores increases, and their connectivity improves. Additionally, the branched chains near the micropores continue to detach, resulting in the formation of meso-macropores with a pore size greater than 2 nm. The connectivity of these meso-macropores is better than that of the micropores. The thermal maturity ranges from 3.5% to 4.3% (with a degree of graphitization of organic matter ranging from 17% to 47.32%). During this stage, the branches of organic matter continue to degrade, leading to the formation of micropores and an improvement in their connectivity. However, the preservation conditions are poor due to the influence of basement fractures. As a result, the gas within the medium macropores is lost, causing a decrease in the pressure of the shale gas reservoir. Consequently, the reservoir is unable to withstand external extrusion stress, ultimately resulting in the collapse or disappearance of the medium macropores.

Author Contributions: Conceptualization, X.S., L.X., and Y.W.; methodology, W.W.; software, Y.Y. (Yingzi Yin); validation, Y.Y. (Yuran Yang) and J.L.; formal analysis, X.Y.; investigation, Y.L.; resources, X.S.; data curation, W.W. and Q.W.; writing—chapter 1–3, X.S.; writing—chapter 4, W.W.; writing—chapter 5 and chapter 6, L.X.; writing—review and editing, Y.W.; visualization, K.Z.; supervision, Y.Y. (Yingzi Yin); project administration, X.S. All authors have read and agreed to the published version of the manuscript.

Funding: This research was funded by the PetroChina Southwest Oil and Gas Field and China University of Petroleum-Beijing cooperative project (Grant No. JS2022-80), China Petroleum Natural Gas Group Co., Ltd. science and technology project ‘the new layer of favorable area optimization and exploration evaluation of key technology research’ (Grant No. 2023ZZ21-04), research project of PetroChina Southwest Oil and Gas Field Company ‘Research on the Enrichment Law of Deep Shale Gas in Luzhou-Yuxi Area’ (Grant No. 20210304-04), and research project of PetroChina Southwest Oil and Gas Field Company ‘Research on controlling factors of shale gas content difference in different tectonic belts in Luzhou-Yuxi area’ (Grant No. 20220304-03).

Data Availability Statement: The data that support the findings of this study are available from the corresponding author upon reasonable request. The data are not publicly available due to privacy.

Acknowledgments: The authors give special thanks to Wang Gaocheng of the PetroChina Zhejiang Oilfield Exploration and Development Research Institute for help with information. In addition, the authors thank the editors and reviewers for their help in revising and improving the article.

Conflicts of Interest: Xuewen Shi, Wei Wu, Liang Xu, Yingzi Yin, Yuran Yang, Jia Liu, Xue Yang, Yanyou Li, Qiuzi Wu, and Kesu Zhong are employees of Shale Gas Research Institute of Petrochina Southwest Oil & Gas Field Company. The paper reflects the views of the scientists and not the company.

References

1. Feng, B.; Yu, J.; Yang, F.; Zhang, Z.; Xu, S. Reservoir characteristics of normally pressured shales from the periphery of Sichuan Basin: Insights into the pore development mechanism. *Energies* **2023**, *16*, 2166. [\[CrossRef\]](#)
2. Nie, H.K.; Li, P.; Dang, W.; Ding, J.H.; Sun, C.X.; Liu, M.; Wang, J.; Du, W.; Zhang, P.X.; Li, D.H.; et al. Enrichment characteristics and exploration directions of deep shale gas of Ordovician-Silurian in the Sichuan Basin and its surrounding areas, China. *Pet. Explor. Dev.* **2022**, *49*, 648–659. [\[CrossRef\]](#)
3. Lan, B.F.; Zhao, F.P.; Li, S.P.; Jiang, H.S.; Liu, S.; Zhang, Z.Y. Investigation of the Enrichment and Accumulation of Normal Pressure Shale Gas in Anchang Syncline Outside of Sichuan Basin. *Front. Earth Sci.* **2022**, *9*, 802142. [\[CrossRef\]](#)
4. Chen, S.B.; Zuo, Z.X.; Zhu, Y.M.; Fu, C.Q.; Zhang, H. Applicability of the testing method for the maturity of organic matter in shale gas reservoirs. *Nat. Gas Geosci.* **2015**, *26*, 564–574.
5. Luo, Q.Y.; Goodarzi, F.; Zhong, N.N.; Wang, Y.; Qiu, N.S.; Skovsted, C.B.; Suchy, V.; Schovsbo, N.H.; Morga, R.; Xu, Y.H.; et al. Graptolites as fossil geo-thermometers and source material of hydrocarbons: An overview of four decades of progress. *Earth-Sci. Rev.* **2019**, *200*, 103000. [\[CrossRef\]](#)
6. Liu, D.H.; Xiao, X.M.; Tian, H.; Min, Y.S.; Zhou, Q.; Cheng, P.; Shen, J.G. Sample maturation calculated using Raman spectroscopic parameters for solid organics: Methodology and geological applications. *Chin. Sci. Bull.* **2013**, *58*, 1228–1241. [\[CrossRef\]](#)
7. Goodarzi, F.; Gentzis, T.; Harrison, C.; Thorsteinsson, R. The significance of graptolite reflectance in regional thermal maturity studies, Queen Elizabeth Islands, Arctic Canada. *Org. Geochem.* **1992**, *18*, 347–357. [\[CrossRef\]](#)
8. Meng, J.H.; Lyu, P.X.; Wu, W.; Pan, R.F.; Zhu, Y.Q. A method for evaluating the thermal maturity of marine shale based on graptolite reflectance and Raman spectroscopy: A case from the Lower Palaeozoic Wufeng-Longmaxi Formations, Southern Sichuan Basin, SW China. *Oil Gas Geol.* **2022**, *43*, 1515–1528.
9. Liu, Y.; Liu, S.M.; Zhang, R.; Zhang, Y. The molecular model of Marcellus shale kerogen: Experimental characterization and structure reconstruction. *Int. J. Coal Geol.* **2021**, *246*, 103833. [\[CrossRef\]](#)
10. Yu, B.; Zhou, R.; Lu, Z.L.; Yu, H.L.; Lu, Y. The preparation method for coal TEM ultrathin sections. *J. Chin. Electron. Microsc. Soc.* **2014**, *33*, 180–187.
11. Houben, M.E.; Barnhoorn, A.; Wasch, L.; Trabuco-Alexandre, J.; Peach, C.J.; Drucy, M.R. Microstructures of Early Jurassic (Toarcian) shales of northern Europe. *Int. J. Coal Geol.* **2016**, *165*, 76–89. [\[CrossRef\]](#)
12. Shi, X.W.; Wu, W.; Hu, H.Y.; Liu, L.H.; Zhu, Y.Q.; Pan, R.F.; Meng, J.H.; Wang, T. The whole apertures of deeply buried Wufeng-Longmaxi formation shale and their controlling factors in Luzhou district, Sichuan Basin. *Earth Sci.* **2023**, *48*, 158–172.
13. Yang, R.; Hao, F.; He, S.; He, C.C.; Guo, X.S.; Yi, J.Z.; Hu, H.Y.; Zhang, S.W.; Hu, Q.H. Experimental investigations on the geometry and connectivity of pore space in organic-rich Wufeng and Longmaxi shales. *Mar. Petrol. Geol.* **2017**, *84*, 225–242. [\[CrossRef\]](#)
14. Tian, H.; Zhang, S.C.; Liu, S.B.; Gao, Y.; Zhang, H.; Wang, M.Z.; Hao, J.Q.; Zheng, Y.P.; Zhang, T. Evolution of pores in shale during thermal maturation using small angle X-ray scattering (SAXS). *Pet. Geol. Exp.* **2016**, *38*, 135–146.
15. Xu, Z.X.; Guo, S.B. Application of NMR and X-CT technology in the pore structure study of shale gas reservoirs. *Adv. Earth Sci.* **2014**, *29*, 624–631.
16. Fan, Y.C.; Liu, K.Y.; Pu, X.G.; Zhao, J.H. Morphological classification and three-dimensional pore structure reconstruction of shale oil reservoirs: A case from the second member of Kongdian formation in the Cangdong sag, Bohai Bay Basin, East China. *Pet. Explor. Dev.* **2022**, *49*, 943–954. [\[CrossRef\]](#)
17. Li, W.H.; Lu, S.F.; Wang, M.; Zhou, N.W.; Cheng, Z.H. Quantitative characterization of micro heterogeneity of tight reservoirs by large-view FE-SEM splicing technology. *Oil Gas Geol.* **2022**, *43*, 1497–1504.
18. Han, Z.H.; Zuo, T.S.; Ma, C.L.; Li, Y.Q.; Cheng, H. Development and prospect of small angle neutron scattering instrument. *WST* **2022**, *44*, 371–391.
19. Ma, Y.; Zhong, N.N.; Huang, X.Y.; Guo, Z.P.; Yao, L.P. The application of focused ion beam scanning electron microscope (FIB-SEM) to the nanometer-sized pores in shales. *J. Chin. Elec. Microsc. Soc.* **2014**, *33*, 251–256.
20. Tang, X.L.; Jiang, S.; Jiang, Z.X.; Li, Z.; He, Z.L.; Long, S.X.; Zhu, D.Y. Heterogeneity of Paleozoic Wufeng-Longmaxi formation shale and its effects on the shale gas accumulation in the Upper Yangtze Region, China. *Fuel* **2019**, *239*, 387–402. [\[CrossRef\]](#)
21. Jiang, Z.X.; Tang, X.L.; Li, Z.; Huang, H.X.; Yang, P.P.; Yang, X.; Li, W.B.; Hao, J. The whole-aperture pore structure characteristics and its effect on gas content of the Longmaxi formation shale in the southeastern Sichuan basin. *ESF* **2016**, *23*, 126–134.
22. Sun, Z.L.; Li, Z.M.; Shen, B.J.; Zhu, Q.M.; Li, C.X. NMR technology in reservoir evaluation for shale oil and gas. *Pet. Geol. Exp.* **2022**, *44*, 930–940.
23. Xue, Z.X.; Jiang, Z.X.; Hao, M.Z.; Tang, X.L.; Li, S.J.; Nie, Z.; Zhong, G.H.; Wu, W.; Liang, Z.K.; Chen, R.H.; et al. Controlling effect of organic matter graphitization on reservoir pore structure in deep shale reservoirs, southern Sichuan. *J. Cent. South Univ. Technol.* **2022**, *53*, 3532–3544.

24. Xue, Z.X.; Jiang, Z.X.; Wang, X.; Gao, Z.Y.; Chang, J.Q.; Nie, Z.; Li, H.; Wu, W.; Qiu, H.Y.; Wang, Q.Y.; et al. Genetic mechanism of low resistivity in high-mature marine shale: Insights from the study on pore structure and organic matter graphitization. *Mar. Petrol. Geol.* **2022**, *144*, 105825. [\[CrossRef\]](#)
25. Fu, Y.H.; Jiang, Y.Q.; Dong, D.Z.; Hu, Q.H.; Lei, Z.A.; Peng, H.; Gu, Y.F.; Ma, S.G.; Wang, Z.M.; Yin, X.P.; et al. Microscopic pore-fracture configuration and gas-filled mechanism of shale reservoirs in the western Chongqing area, Sichuan Basin, China. *Pet. Explor. Dev.* **2021**, *48*, 916–927. [\[CrossRef\]](#)
26. Sun, X.L.; Zhang, X.G.; Lin, C.Y.; Zhao, Z.X.; Ma, C.F.; Lin, J.L. Quantitative Evaluation method of HPMI pore-throat distribution based on NMR calibration. *RMA* **2017**, *36*, 601–607.
27. Jiang, Z.X.; Li, X.; Wang, X.M.; Wang, G.Z.; Qiu, H.Y.; Zhu, D.Y.; Jiang, H.Y. Characteristic differences and controlling factors of pores in typical South China shale. *Oil Gas Geol.* **2021**, *42*, 41–53.
28. Nie, H.K.; Sun, C.X.; Liu, G.X.; Du, W.; He, Z.L. Dissolution pore types of the Wufeng Formation and the Longmaxi Formation in the Sichuan Basin, south China: Implications for shale gas enrichment. *Mar. Petrol. Geol.* **2019**, *201*, 243–251. [\[CrossRef\]](#)
29. Li, X.; Jiang, Z.X.; Song, Y.; Zhai, G.Y.; Bao, S.J.; Li, Z.; Tang, X.L.; Wang, P.F.; Li, T.W.; Wang, G.Z.; et al. Porosity evolution mechanisms of marine shales at over-maturity stage: Insight from comparable analysis between Lower Cambrian and Lower Silurian inside and at the margin of the Sichuan Basin, South China. *Interpretation* **2018**, *6*, T739–T757. [\[CrossRef\]](#)
30. Gou, Q.Y.; Xu, S.; Hao, F.; Yang, F.; Shu, Z.G.; Liu, R. The effect of tectonic deformation and preservation condition on the shale pore structure using adsorption-based textural quantification and 3D image observation. *Energy* **2021**, *219*, 119579. [\[CrossRef\]](#)
31. Shen, C.B.; Mei, L.F.; Xu, Z.P.; Tang, J.G. Architecture and Tectonic evolution of composite basin-mountain system in Sichuan Basin and its adjacent areas. *Geotect. Metallog.* **2007**, *3*, 288–299.
32. Sun, S.C.; Guo, D.B.; Li, L.X.; Li, J.L.; Gao, S.L.; Su, S.; Zhang, B. Characteristics of terrestrial heat flows and types of thermal reservoir systems in the Sichuan Basin. *Nat. Gas Ind.* **2022**, *42*, 21–34.
33. Jiang, Z.X.; Song, Y.; Tang, X.L.; Li, Z.; Wang, X.M.; Wang, G.Z.; Xue, Z.X.; Li, X.; Zhang, K.; Chang, J.Q.; et al. Controlling factors of marine shale gas differential enrichment in southern China. *Pet. Explor. Dev.* **2020**, *47*, 617–628. [\[CrossRef\]](#)
34. Duan, X.G.; Wu, Y.H.; Jiang, Z.X.; Hu, Z.M.; Tang, X.L.; Zhang, Y.; Wang, X.L.; Chen, W.Y. A new method for predicting the gas content of low-resistivity shale: A case study of Longmaxi shale in southern Sichuan Basin, China. *Energies* **2023**, *16*, 6169. [\[CrossRef\]](#)
35. Ma, S.J.; Zeng, L.B.; Shi, X.W.; Wu, W.; Tian, H.; Xue, M.; Luo, L. Characteristics and main controlling factors of natural fractures in marine shale in luzhou area, Sichuan Basin. *Earth Sci.* **2023**, *48*, 2630–2642.
36. Wang, E.; Meng, K.; Su, Z.; Meng, Q.R.; Chu, J.J.; Chen, Z.L.; Wang, G.; Shi, X.H.; Liang, X.Q. Block rotation: Tectonic response of the Sichuan Basin to the southeastward growth of the Tibetan plateau along the Xianshuihe-Xiaojiang fault. *Tectonics* **2014**, *33*, 686–718. [\[CrossRef\]](#)
37. Wang, H.Y.; Shi, Z.S.; Sun, S.S.; Zhao, Q.; Zhou, T.Q.; Cheng, F.; Bai, W.H. Microfacies types and distribution of epicontinental shale: A case study of the Wufeng-Longmaxi shale in southern Sichuan Basin, China. *Pet. Explor. Dev.* **2023**, *50*, 51–64. [\[CrossRef\]](#)
38. Liang, F.; Zhao, Q.; Shi, X.W.; Wang, Y.M.; Zhang, Q.; Zhou, S.W.; Qi, L.; Cui, H.Y. A new method for isochronous stratigraphic division of Longmaxi Formation in Sichuan Basin, China. *Acta Pet. Sin.* **2023**, *44*, 1274–1298.
39. Li, Y.; He, J.H.; Deng, H.C.; Ma, R.L.; Wang, K.Y.; Li, R.X.; Zhao, Y.Q.; Tang, J.M.; Chen, X.H. Pore Structure characterization and its influencing factors in favorable lithofacies of normal pressure shale reservoirs: A case study of Wufeng-Longmaxi formations in Lintanchang Area, Southeast Sichuan Basin. *Nat. Gas Geosci.* **2023**, *34*, 1274–1288.
40. Tian, C.; Li, Y.; Li, D.Y.; Zhang, W.; Zhong, K.S.; Zhou, S.W.; Luo, C.; Jiang, W.B.; Li, D.; He, L.; et al. Selection and recommendation of shale reservoir porosity measurement methods. *Nat. Gas Ind.* **2023**, *43*, 57–65.
41. Ji, W.M.; Song, Y.; Jiang, Z.X.; Chen, L.; Wang, P.F.; Liu, Q.X.; Gao, F.L.; Yang, X. Micro-nano pore structure characteristics and its control factors of shale in Longmaxi Formation, southeastern Sichuan Basin. *Acta Pet. Sin.* **2016**, *37*, 182–195.
42. Wang, Q.; Xu, X.C.; Chi, M.S.; Zhang, H.X.; Cui, D.; Bai, J.R. FTIR study on composition of oil shale kerogen and its pyrolysis oil generation characteristics. *J. Fuel Chem. Technol.* **2015**, *43*, 1158–1166.
43. Jiang, P.F.; Wu, J.F.; Zhu, Y.Q.; Zhang, D.K.; Wu, W.; Zhang, R.; Wu, Z.; Wang, Q.; Yang, Y.R.; Yang, X.; et al. Enrichment conditions and favorable areas for exploration and development of marine shale gas in Sichuan Basin. *Acta Pet. Sin.* **2023**, *44*, 91–109.
44. Gai, H.F.; Tian, H.; Cheng, P.; He, C.M.; Wu, Z.J.; Ji, S.; Xiao, X.M. Characteristics of molecular nitrogen generation from overmature black shales in South China: Preliminary implications from pyrolysis experiments. *Mar. Petrol. Geol.* **2020**, *120*, 104527. [\[CrossRef\]](#)

Disclaimer/Publisher’s Note: The statements, opinions and data contained in all publications are solely those of the individual author(s) and contributor(s) and not of MDPI and/or the editor(s). MDPI and/or the editor(s) disclaim responsibility for any injury to people or property resulting from any ideas, methods, instructions or products referred to in the content.